THE LARGEST M DWARFS FLARES FROM ASAS-SN

Sarah J. Schmidt,[1] Benjamin J. Shappee,[2, 3, 4, 5] Jennifer L. van Saders,[2, 4, 5] K. Z. Stanek,[6, 7] Jonathan S. Brown,[6] C. S. Kochanek,[6, 7] Subo Dong,[8] Maria R. Drout,[3, 9, 5] Stephan Frank,[6] T. W.-S. Holoien,[10, 5] Sean Johnson,[3, 4, 11] Barry F. Madore,[5] J. L. Prieto,[12, 13] Mark Seibert,[5] Marja K. Seidel,[5, 14] and Gregory V. A. Simonian[6]

[1] Leibniz-Institute for Astrophysics Potsdam (AIP), An der Sternwarte 16, 14482, Potsdam, Germany
[2] Institute for Astronomy, University of Hawai'i, 2680 Woodlawn Drive, Honolulu, HI 96822, USA
[3] Hubble Fellow
[4] Carnegie-Princeton Fellow
[5] The Observatories of the Carnegie Institution for Science, 813 Santa Barbara St., Pasadena, CA 91101, USA
[6] Department of Astronomy, The Ohio State University, 140 West 18th Avenue, Columbus, OH 43210, USA
[7] Center for Cosmology and Astroparticle Physics, The Ohio State University, 191 W. Woodruff Avenue, Columbus, OH 43210
[8] Kavli Institute for Astronomy and Astrophysics, Peking University, Yi He Yuan Road 5, Hai Dian District, Beijing 100871, China
[9] Carnegie-Dunlap Fellow
[10] Carnegie Fellow
[11] Department of Astrophysics, Princeton University, Princeton, NJ, USA
[12] Núcleo de Astronomía de la Facultad de Ingeniería y Ciencias, Universidad Diego Portales, Av. Ejército 441, Santiago, Chile
[13] Millennium Institute of Astrophysics, Santiago, Chile
[14] Caltech-IPAC, Spitzer Science Center, 1200 E. California Blvd., Pasadena, CA 91125 USA

ABSTRACT

The All-Sky Automated Survey for Supernovae (ASAS-SN) is the only project in existence to scan the entire sky in optical light every $\sim$day, reaching a depth of $g \sim 18$ mag. Over the course of its first four years of transient alerts (2013-2016), ASAS-SN observed 53 events classified as likely M dwarf flares. We present follow-up photometry and spectroscopy of all 53 candidates, confirming flare events on 47 M dwarfs, one K dwarf, and one L dwarf. The remaining four objects include a previously identified TT Tauri star, a young star with outbursts, and two objects too faint to confirm. A detailed examination of the 49 flare star light curves revealed an additional six flares on five stars, resulting in a total of 55 flares on 49 objects ranging in V-band contrast from $\Delta V = -1$ to -10.2 mags. Using an empirical flare model to estimate the unobserved portions of the flare light curve, we obtain lower limits on the V-band energy emitted during each flare, spanning $\log(E_V/\mathrm{ergs}) = 32$ to 35, which are among the most energetic flares detected on M dwarfs. The ASAS-SN M-dwarf flare stars show a higher fraction of Hα emission as well as stronger Hα emission compared to M dwarfs selected without reference to activity, consistent with belonging to a population of more magnetically active

sjschmidt@aip.de

stars. We also examined the distribution of tangential velocities, finding that the ASAS-SN flaring M dwarfs are likely to be members of the thin disk and are neither particularly young nor old.

Keywords: stars: chromospheres – stars: low-mass – stars: late-type

1. INTRODUCTION

Stellar flares are dramatic multi-wavelength outbursts that originate in the reconnection of magnetic field lines at the surfaces of stars across the main sequence. A typical flare event stretches from the stellar photosphere to the corona, with high energy particle acceleration dominating radio and X-ray flare emission (e.g., Lin & Hudson 1976; Osten et al. 2005), while dense, hot material in the pre-flare photosphere and chromosphere emits at UV and optical wavelengths through a combination of thermal blackbody and atomic emission (e.g., Hawley & Pettersen 1991; Kowalski et al. 2013). Most flares are rapid transients, characterized by an initial impulsive rise and decay (lasting a few to tens of minutes) followed by a more gradual exponential decay (typically lasting hours; see e.g., Davenport et al. 2014a). Flares are often observed on M dwarfs, both because these low-mass stars remain magnetically active and flaring even at ages of a few Gyr (West et al. 2008; Hilton et al. 2010; Pineda et al. 2013), and because the contrast of the hot ($\sim$10000 K), blue thermal component of the flare emission with the cool ($\sim$3000 K), red photosphere allows for observations of modest ($E \sim 10^{26}$ ergs) flares that require high precision photometry to detect on solar-type stars other than the Sun. So far, M dwarf flares have been observed to span a wide range of energies, from $E \sim 10^{26}$ ergs up to 10^{35}–10^{36} ergs (Lacy et al. 1976; Kowalski et al. 2010; Davenport 2016).

When a single star is observed long enough that a significant number of flares are detected (tens to hundreds), the energies of those flares follow a flare frequency distribution (FFD) where the most energetic flares occur far more rarely than lower energy flares (Lacy et al. 1976). FFDs have been found to depend on stellar spectral type (a proxy for mass and surface temperature) as well as other indicators of stellar activity due to a dependence on the underlying magnetic field strength (Hilton 2011; Hawley et al. 2014). The dynamo that generates stellar magnetic fields (and thus flares) depends strongly on the rotation rate of the stars, both above and below the fully convective boundary (Browning et al. 2006; Browning 2008). As stars age, their rotational energy is dissipated through a combination of a steady stellar winds and transient magnetic emission events, leading to weaker magnetic fields and net lower magnetic activity. A well-measured flare frequency distribution across a range of masses, ages, and metallicities would be an important step in understanding the magnetic evolution of M dwarfs and other main sequence stars.

Powerful flares can also present a challenge to the surface habitability of exoplanets that orbit M dwarf hosts. The habitable zones (where liquid water can persist on the surface of a rocky planet) of M dwarfs are 10–100 times closer to their host star than that of the Sun (Luger & Barnes 2015), so the UV emission observed from most flares will have a stronger effect on planets around M dwarfs. UV emission, if too intense, can first deplete the outer ozone layer and then pass through an exoplanet atmosphere to destroy DNA and other essential molecules. On early- to mid-M dwarfs, UV emission alone is not strong enough to hinder life dramatically, either during quiescence (France et al. 2016) or during a single flare Segura et al. (2010). On later M dwarfs (O'Malley-James & Kaltenegger 2017) or M dwarfs with a high rate of large flares (Tilley et al. 2017), the UV emission from those flares may play a role in depleting the upper ozone of an oxygen atmosphere but is unlikely to destroy it completely.

The observed UV emission from flares may not prevent growth of life around M dwarfs, but powerful flares are often accompanied by ener-

getic particles, either emitted as a particle beam or released as part of a coronal mass ejection (CME); these CMEs could have dramatic effects on the atmospheres of otherwise habitable planets (Khodachenko et al. 2007; Lammer et al. 2007). Outside our Solar system, there are no observations of particle beams and only a handful of observations that could be consistent with CMEs (e.g., Vida et al. 2016), but scaling from correlations between Solar flares and these energetic ejections indicates that M dwarf planets would be hit by strong particle beams multiple times per day (Kay et al. 2016; Youngblood et al. 2017) and that those events could work together to deplete the ozone (Tilley et al. 2017). Because these results rely on extrapolating known flare rates to estimate particle events, it is essential to determine flare rates as a function of stellar mass and age to calculate the effect on a wider range of planets orbiting M dwarfs over a large range of spectral types and ages.

The *Kepler* mission (Borucki et al. 2010) and its extension into K2 (Howell et al. 2014) have proven to be an essential resource for flare observations at optical wavelengths. While the relatively red pass-band of the *Kepler* space craft is not ideal for observing the blue/UV wavelengths where the flare and photosphere contrast is highest, the precision and cadence ($\sim$1 minute) of the photometry has enabled the detection of large numbers of stellar flares. Results from *Kepler* include catalogs of flares across the main sequence (Davenport 2016; Walkowicz et al. 2011), superflares ($E > 10^{33}$ ergs) on Solar-type stars (Maehara et al. 2012), detailed analyses of the many M dwarf flares (Hawley et al. 2014; Ramsay & Doyle 2015; Silverberg et al. 2016), and the first observations of white-light flares on an L dwarf (Gizis et al. 2013). While data from *Kepler* are ideal for detailed time-series analysis of flares, the mission is limited due to the need to pre-

select a limited number of targets in each quarter and field. Most stars are observed because they are likely to be particularly good targets for exoplanet searches, and the Kepler/K2 stars are not representative of the underlying population of M dwarfs. To assess the complete flare rate across an unbiased sample of stars, a different approach is needed.

The All-Sky Automated Survey of Supernovae (ASAS-SN; Shappee et al. 2014) is a survey with the main objective of detecting the nearest, brightest supernovae in the Universe (Shappee et al. 2016b; Holoien et al. 2017b,c,a), that has proven to be a valuable resource for a variety of transient events both inside and outside our Galaxy, including the three brightest optical tidal disruption events (Holoien et al. 2014b, 2016b,a), the most luminous SN (Dong et al. 2016), AGN flares (Shappee et al. 2014), dramatic variability on young stars (Holoien et al. 2014b; Herczeg et al. 2016), novae (Li et al. 2017), and cataclysmic variables (Davis et al. 2015). ASAS-SN has already found very strong flares on M dwarfs (e.g., Stanek et al. 2013a; Schmidt et al. 2014; Simonian et al. 2016; Rodríguez et al. 2018) and the strongest L dwarf flare (Schmidt et al. 2016). Because of its relatively bright magnitude range, flaring M dwarfs detected with ASAS-SN are primarily bright, nearby M dwarfs that can be examined in detail more easily than those in deeper surveys like LSST or Pan-STARRS. These flare detections are thus useful both for understanding nearby M dwarfs and for classifying flares in future time-domain surveys.

We describe the selection of flare candidates in ASAS-SN (Section 2) and our follow-up observations (Section 3). We then characterize the flares in Section 4 and their stars in Section 5. In Section 6, we discuss individual objects of interest and we summarize our results in Section 7.

2. ASAS-SN FLARE DETECTIONS AND SAMPLE SELECTION

The ASAS-SN survey is a long-term project to monitor the entire sky for bright transient objects with as fast a cadence as possible. ASAS-SN began taking data in November 2011 with two cameras in Hawaii and in April 2013 began searching for transients in real time. Since 2013, ASAS-SN has expanded multiple times, as detailed by Holoien et al. (2017c) and Kochanek et al. (2017). The data for the M dwarfs examined here were taken while ASAS-SN was taking data only at the original two sites at Hawaii and Chile. Each ASAS-SN unit now consists of four 14-cm aperture Nikon telephoto lenses on a common mount allowing the two ASAS-SN units used in this study to cover ∼16,000 deg^2 every clear night to $V \approx 16.5 - 17.3$ mag, depending on lunation. This allowed us to scan the visible (Sun constrained) sky every two nights. ASAS-SN currently has five robotic units distributed adding units to sites in Chile, Texas, and South Africa and we will add a sixth unit in China by the end of 2018. We currently observe the entire visible sky every 20 hours to $g \approx 18.5$ mag.

The telescopes are scheduled automatically and the data are reduced in real-time. Our transient detection pipeline typically identifies new transient sources less than an hour after the data are taken. Candidates are then scanned by team members in North America, South America, Asia and Europe to determine if the sources are likely real, and to provide a rough classification based on public survey photometry, literature measurements where available, and the previous ASAS-SN light curve at that location. Transient events that are determined to be real are immediately made public on the ASAS-SN transients page[1]. SNe and CV outbursts are the most common detections, including 500+ and 1250+ candidates as of the end of 2016.

When we first retrieved our target list on 2016 April 6, the ASAS-SN transient list included 1518 total transients, 48 of which were flagged as possible M dwarf flares. Of those, five were published in Astronomer's Telegrams (Stanek et al. 2013a,b; Holoien et al. 2014a; Shappee et al. 2016a; Simonian et al. 2016), and two had been examined in detail (Schmidt et al. 2014, 2016). To perform a check on the completeness of the identification of ASAS-SN transient events as flares on M dwarfs, we queried the Sloan Digital Sky Survey (SDSS Aihara et al. 2011; York et al. 2000), Two Micron All Sky Survey (2MASS Skrutskie et al. 2006), and Wide-field Infrared Survey Explorer (WISE Wright et al. 2010) photometric databases. We color-selected objects at the positions of ASAS-SN transients that were likely to be M dwarfs based on their $i - z$ colors (when SDSS photometry was available) or their 2MASS and WISE colors (when SDSS photometry was not available). SDSS and 2MASS photometry were subject to the color and quality cuts described in Schmidt et al. (2015), and $rizK_S$ magnitudes are included in Table 1. We recovered 25 of the 48 candidates and identified an additional 11 candidates. The 23 transient events originally identified as flares on M dwarfs but not recovered in our search were either missing some data in the ASAS-SN transients page or were flagged for faintness or saturation in one of the surveys. The additional 11 candidates recovered were very similar to M dwarfs, but were classified by ASAS-SN as CV outbursts and/or had red $J - W2$ colors consistent with young accreting stars. We retained the brightest two of those objects (ASASSN-15ep and ASASSN-15af) as a check on the initial classifications.

We also added six additional candidate flaring M dwarfs that were observed between 2016

---

[1] http://www.astronomy.ohio-state.edu/asassn/transients.html

Table 1. Properties of ASAS-SN Flare Dwarfs

ASAS-SN ID	Spectral Type	$H\alpha$ EW (Å)	V	R	I	r	i	z	K_S
13ba	M6	8.4 ± 0.1	17.42 ± 0.01	15.91 ± 0.02	14.21 ± 0.01	16.76 ± 0.02	$\cdots$	13.99 ± 0.02	11.45 ± 0.02
13be	M4	3.2 ± 1.2	18.40 ± 0.01	17.16 ± 0.01	15.58 ± 0.04	17.83 ± 0.01	16.31 ± 0.01	15.48 ± 0.03	13.31 ± 0.04
13bf	M2	2.7 ± 0.1	17.22 ± 0.01	16.19 ± 0.01	15.12 ± 0.01	16.60 ± 0.01	15.70 ± 0.03	15.21 ± 0.03	13.10 ± 0.04
13bg	M6	3.6 ± 0.2	17.13 ± 0.01	15.53 ± 0.01	13.91 ± 0.01	16.51 ± 0.01	14.61 ± 0.02	13.54 ± 0.02	10.95 ± 0.02
13bh	M5	5.8 ± 0.8	16.71 ± 0.05	15.53 ± 0.02	13.88 ± 0.03	$\cdots$	$\cdots$	$\cdots$	11.70 ± 0.02
13bi	M4	1.3 ± 0.1	18.08 ± 0.01	16.67 ± 0.01	15.11 ± 0.01	17.40 ± 0.01	15.87 ± 0.01	15.02 ± 0.01	12.69 ± 0.03
13bk	M6	29.1 ± 2.1	18.68 ± 0.01	17.36 ± 0.02	15.65 ± 0.01	18.06 ± 0.02	16.43 ± 0.02	15.54 ± 0.02	13.17 ± 0.04
13bl	M3	5.6 ± 0.1	14.83 ± 0.01	13.63 ± 0.01	12.18 ± 0.01	14.15 ± 0.01	$\cdots$	12.14 ± 0.02	9.98 ± 0.02
13bn	M4	5.0 ± 0.3	17.16 ± 0.02	15.88 ± 0.01	14.39 ± 0.02	16.48 ± 0.01	15.06 ± 0.01	14.28 ± 0.01	11.94 ± 0.02
13bt	M7	4.5 ± 0.0	19.14 ± 0.06	17.55 ± 0.06	15.67 ± 0.01	18.68 ± 0.02	16.55 ± 0.01	15.42 ± 0.02	12.78 ± 0.03
13cb	M8	26.8 ± 0.5	21.83 ± 0.40	$\cdots$	$\cdots$	21.23 ± 0.05	18.65 ± 0.02	17.08 ± 0.02	13.91 ± 0.05
13cm	M4	6.1 ± 2.3	16.21 ± 0.03	$\cdots$	13.23 ± 0.04	15.41 ± 0.02	$\cdots$	13.07 ± 0.02	10.74 ± 0.02
13cr	M4	7.0 ± 1.5	14.82 ± 0.02	13.63 ± 0.01	12.20 ± 0.01	$\cdots$	$\cdots$	$\cdots$	9.69 ± 0.02
13de	M4	7.4 ± 1.0	18.14 ± 0.02	$\cdots$	15.18 ± 0.03	17.57 ± 0.02	16.03 ± 0.02	15.20 ± 0.02	12.84 ± 0.03
13di	M5	5.1 ± 0.1	19.97 ± 0.06	18.78 ± 0.05	17.05 ± 0.06	$\cdots$	$\cdots$	$\cdots$	14.80 ± 0.11
13dj	M2	<0.75	23.09 ± 0.04	21.80 ± 0.02	20.49 ± 0.02	22.59 ± 0.18	21.22 ± 0.08	20.20 ± 0.14	$\cdots$
13dk	M5	7.8 ± 3.9	19.91 ± 0.02	18.37 ± 0.02	16.74 ± 0.02	19.17 ± 0.02	17.53 ± 0.02	16.63 ± 0.02	14.33 ± 0.05
14bj	M4	2.6 ± 0.6	19.73 ± 0.01	18.32 ± 0.01	16.71 ± 0.01	19.13 ± 0.01	17.52 ± 0.02	16.63 ± 0.02	14.34 ± 0.07
14bm	M5	6.5 ± 0.8	20.47 ± 0.01	18.95 ± 0.01	17.28 ± 0.01	19.75 ± 0.02	18.07 ± 0.02	17.15 ± 0.02	14.62 ± 0.10
14bn	M4	4.5 ± 1.2	17.40 ± 0.04	$\cdots$	14.23 ± 0.01	$\cdots$	$\cdots$	$\cdots$	12.16 ± 0.02
14cx	M6	8.2 ± 0.8	19.62 ± 0.02	17.96 ± 0.02	16.24 ± 0.03	$\cdots$	$\cdots$	$\cdots$	13.50 ± 0.03
14dv	M6	10.3 ± 0.7	20.72 ± 0.01	18.70 ± 0.08	17.15 ± 0.09	$\cdots$	$\cdots$	$\cdots$	14.60 ± 0.08
14ea	M5	9.5 ± 0.1	15.78 ± 0.01	14.38 ± 0.01	13.01 ± 0.01	15.22 ± 0.01	$\cdots$	12.61 ± 0.02	10.20 ± 0.02
14fi	M5	5.6 ± 1.9	17.21 ± 0.03	$\cdots$	14.11 ± 0.04	$\cdots$	$\cdots$	$\cdots$	11.82 ± 0.02
14gj	M5	8.5 ± 0.6	20.63 ± 0.05	18.95 ± 0.03	17.05 ± 0.04	$\cdots$	$\cdots$	$\cdots$	14.58 ± 0.08
14gn	M5	6.7 ± 1.3	21.38 ± 0.04	19.68 ± 0.02	17.98 ± 0.02	20.57 ± 0.04	18.76 ± 0.02	17.78 ± 0.02	15.03 ± 0.13
14hc	K5	<0.75	18.99 ± 0.02	17.59 ± 0.02	15.80 ± 0.03	18.30 ± 0.01	16.59 ± 0.01	15.65 ± 0.01	13.26 ± 0.03
14hz	M6	6.9 ± 1.0	20.16 ± 0.02	18.66 ± 0.08	17.16 ± 0.12	$\cdots$	$\cdots$	$\cdots$	14.56 ± 0.08
14ji	M7	10.1 ± 5.0	22.42 ± 0.05	20.35 ± 0.02	18.41 ± 0.01	21.54 ± 0.07	19.30 ± 0.02	17.99 ± 0.03	15.05 ± 0.14
14jw	M7	6.4 ± 0.2	18.96 ± 0.06	17.34 ± 0.04	15.46 ± 0.04	$\cdots$	$\cdots$	$\cdots$	12.36 ± 0.03
14jy	M4	4.8 ± 0.3	15.05 ± 0.01	$\cdots$	$\cdots$	$\cdots$	$\cdots$	$\cdots$	10.12 ± 0.02
14ke	M8	16.4 ± 7.3	21.03 ± 0.04	19.38 ± 0.07	17.60 ± 0.03	$\cdots$	$\cdots$	$\cdots$	14.33 ± 0.08
14lc	M9	20.0 ± 0.3	24.20 ± 0.10	21.44 ± 0.03	19.29 ± 0.02	$\cdots$	$\cdots$	$\cdots$	15.17 ± 0.12
14mz	M6	5.0 ± 0.0	19.38 ± 0.02	17.68 ± 0.02	15.82 ± 0.03	18.73 ± 0.02	16.73 ± 0.02	15.64 ± 0.02	13.07 ± 0.03
15ep	M5	6.8 ± 2.8	19.66 ± 0.03	$\cdots$	16.40 ± 0.05	$\cdots$	$\cdots$	$\cdots$	13.88 ± 0.06
15kl	M3	2.7 ± 0.4	17.21 ± 0.04	15.92 ± 0.06	14.29 ± 0.07	$\cdots$	$\cdots$	$\cdots$	11.73 ± 0.02
15ll	M4	<0.75	22.60 ± 0.03	21.34 ± 0.01	19.91 ± 0.01	22.12 ± 0.09	20.75 ± 0.04	19.82 ± 0.08	$\cdots$
15oy	M8	9.2 ± 0.3	18.63 ± 0.01	16.54 ± 0.01	14.55 ± 0.01	23.73 ± 1.23	24.36 ± 61.59	21.84 ± 3.38	11.26 ± 0.02
15tv	M5	6.6 ± 0.0	19.66 ± 0.01	18.24 ± 0.02	16.44 ± 0.01	18.96 ± 0.02	17.21 ± 0.02	16.27 ± 0.02	13.83 ± 0.04
16ae	L0	26.4 ± 0.2	23.05 ± 0.43	$\cdots$	19.43 ± 0.03	$\cdots$	20.75 ± 0.05	18.87 ± 0.04	15.47 ± 0.21
16cx	M9	6.3 ± 0.2	22.67 ± 0.42	$\cdots$	$\cdots$	22.07 ± 0.12	19.30 ± 0.02	17.67 ± 0.02	14.68 ± 0.09
16di	M7	6.6 ± 2.9	20.36 ± 0.01	18.54 ± 0.01	16.72 ± 0.01	19.68 ± 0.02	17.59 ± 0.01	16.35 ± 0.02	13.48 ± 0.05
16dj	M4	6.1 ± 0.2	16.03 ± 0.01	14.76 ± 0.01	13.16 ± 0.01	15.30 ± 0.02	13.85 ± 0.02	13.01 ± 0.02	10.81 ± 0.02
16dr	M5	6.1 ± 1.4	19.60 ± 0.02	17.84 ± 0.03	15.91 ± 0.04	18.96 ± 0.02	16.84 ± 0.01	15.70 ± 0.01	13.03 ± 0.03
16du	M6	5.6 ± 0.1	21.80 ± 0.07	20.37 ± 0.02	18.37 ± 0.01	21.34 ± 0.06	19.16 ± 0.02	18.08 ± 0.03	15.42 ± 0.16
16gt	M6	4.9 ± 0.4	17.09 ± 0.02	$\cdots$	13.56 ± 0.05	$\cdots$	$\cdots$	$\cdots$	11.12 ± 0.02
16hq	M8	9.3 ± 1.7	21.55 ± 0.02	19.27 ± 0.01	17.13 ± 0.01	$\cdots$	$\cdots$	$\cdots$	13.64 ± 0.04
16kq	M4	4.5 ± 0.9	18.17 ± 0.01	$\cdots$	15.10 ± 0.01	17.44 ± 0.01	15.92 ± 0.01	15.08 ± 0.01	12.81 ± 0.03
GJ3039	M4	5.0 ± 0.1	12.66 ± 0.01	$\cdots$	$\cdots$	$\cdots$	$\cdots$	$\cdots$	11.82 ± 0.02

April and 2016 October, for a total list of 55 candidate flaring M dwarfs. Of those, two (ASASSN-13cn and ASASSN-14bk) were not observed because they fell outside color cuts designed to limit the sample to M dwarfs. Our final target list of 53 objects is given in Table 2.

3. OBSERVATIONS

We obtained follow-up optical photometry and spectroscopy to characterize the host stars of the 53 candidate M dwarfs and flare events detected by ASAS-SN.

3.1. *Photometry*

We obtained follow-up VRI photometry for the majority of our sources, both to aid in source classification (combined with survey photometry) and to provide quiescent V-band measurements to compare to the V-band flare detections. Typically, the photometry was obtained when acquiring sources for spectroscopic observations. We obtained optical imaging using the Inamori-Magellan Areal Camera & Spectrograph (IMACS; Dressler et al. 2011) on the Baade-Magellan 6.5-m telescope, the Ohio State Multi-Object Spectrograph (OS-MOS; Martini et al. 2011) on the MDM Observatory Hiltner 2.4-m telescope, and the Wide Field Reimaging CCD Camera (WFCCD) on the Irénée du Pont 100-inch Telescope. All data were reduced with standard routines in the IRAF `ccdred` package. We performed aperture photometry on the reduced images using the IRAF `apphot` package. The data were calibrated using Sloan Digital Sky Survey (SDSS; York et al. 2000) Data Release 7 (Abazajian et al. 2009) data when available and using the AAVSO Photometric All-Sky Survey (APASS; Henden & Munari 2014) when SDSS was unavailable. When using SDSS, the Sloan filters were transformed onto the Johnson-Cousins magnitude system using transforma-

tions presented by Robert Lupton[2]. The resulting photometry is presented in Table 1.

We initially identified flares based on quick photometry from ASAS-SN images. To examine the lightcurves in more detail, we performed aperture photometry at the location of each flare as described in Kochanek et al. (2017). Briefly, the photometry is done using the IRAF apphot package and calibrated to APASS (Henden & Munari 2014). However, for ASASSN-13be there is a nearby blended star and so we performed aperture photometry on subtracted images, calibrated to APASS, and then added back in the quiescent flux as measured from our higher resolution OSMOS images. We also examined the ASAS-SN light curve for each source to look for additional flares and to characterize the flares detected by ASAS-SN (see Section 4). In addition to the original flares that triggered an ASAS-SN classification, we detected six additional significant ($\Delta V < -1.0$) flares on five stars, which we include in our analysis. The photometry of each flare along with 3-sigma upper limits for images within ∼24 hours of each flare event are presented in Table 3.

3.2. *Spectroscopy*

To confirm the stellar nature of the M dwarf candidates and to characterize them in terms of spectral type and quiescent chromospheric activity (through the Hα emission line), we obtained low-resolution (R∼2000–4000) optical (6000–8000Å) spectra from a variety of telescopes. The instruments and telescopes used for each target are listed in Table 2. We adopted the spectra for ASASSN-13cb and ASASSN-16ae described by Schmidt et al. (2014) and Schmidt et al. (2016), respectively.

We obtained optical spectroscopy for bright southern sources on the Irénée du Pont tele-

---

[2] `http://www.sdss.org/dr5/algorithms/sdssUBVRITransform`

Table 2. Observation Log

ASAS-SN			Spectroscopy		Photometric
Number	RA	dec	Telescope/Instr	ET (s)	Bands
13ba	01 17 00.6	-05 06 04.6	Magellan/Baade	2 x 300	VRI
13be	18 04 08.7	+46 56 04.0	MDM	4 x 1800	VRI
13bf	23 06 12.9	-09 42 33.2	Magellan/Baade	2 x 300	VRI
13bg	23 54 22.4	+07 02 48.7	Magellan/Baade	1 x 450	VRI
13bh	01 35 13.7	+18 23 13.9	MDM	3 x 1200	VRI
13bi	14 58 05.5	+02 44 33.6	Magellan/Baade	2 x 600	VRI
13bk	17 08 56.9	+71 51 48.1	MDM	4 x 1800	VRI
13bl	17 28 39.7	+28 25 35.4	MDM	2 x 900	VRI
13bn	23 54 03.3	+37 56 52.6	MDM	3 x 1200	VRI
13bt	15 53 26.1	+48 08 59.4	LBT	2 x 6 x 800	VRI
13cm	01 46 51.4	-16 52 19.7	du Pont	1 x 1500	VI
13cr	04 36 49.2	-02 49 29.7	MDM	2 x 1200	VRI
13de	04 16 23.4	-05 17 27.9	du Pont	4 x 1800	VI
			MDM	1 x 1800	
13di	07 14 51.8	+64 27 02.2	LBT	2 x 4 x 750	VRI
13dj	01 38 15.5	+16 39 43.1	Magellan/Baade	7 x 1800	VRI
13dk	09 46 23.8	+19 55 10.6	Magellan/Baade	1 x 1500 + 1 x 1800	VRI
14aa	09 18 51.4	+19 27 33.6	Magellan/Baade	3 x 2500	VRI
14be	11 31 24.9	+04 41 16.5	Magellan/Baade	5 x 2500	VRI
14bj	14 49 37.7	+16 56 56.9	Magellan/Baade	2 x 1200	VRI
14bm	14 22 13.3	+03 03 04.2	Magellan/Baade	2 x 1200	VRI
14bn	01 22 42.7	-29 11 18.4	du Pont	5 x 1800	VI
14cx	18 04 00.0	+20 56 46.2	Magellan/Baade	2 x 750	VRI
14dv	01 50 38.4	-24 23 56.4	Magellan/Baade	2 x 1200	VRI
14ea	21 55 17.5	-00 45 49.3	Magellan/Baade	2 x 300	VRI
14fi	02 03 32.9	-67 31 26.8	du Pont	3 x 1500	VI
14gj	03 12 15.7	+26 04 40.6	Magellan/Baade	3 x 800	VRI
14gn	23 10 11.1	+24 02 17.1	Magellan/Baade	3 x 1200	VRI
14hc	23 55 51.1	+24 48 51.9	MDM	6 x 1800	VRI
14hz	20 45 26.6	-34 03 39.9	Magellan/Baade	2 x 1200	VRI
14ji	04 05 51.4	-11 19 17.0	Magellan/Baade	4 x 1500	VRI
14jw	21 47 18.3	-41 16 20.8	Magellan/Baade	2 x 600	VRI
14jy	07 06 58.9	-62 21 10.9	du Pont	2 x 750	VI
14ke	02 19 08.2	+11 07 45.9	Magellan/Baade	3 x 1200	VRI
14lc	12 02 29.6	+24 12 12.4	LBT	2 x 4 x 1500	VRI
14mz	08 51 13.9	+19 12 21.5	LBT	2 x 3 x 800	VRI
15af	01 57 54.9	-54 30 37.9	Magellan/Baade	1 x 600	VRI
			du Pont	1 x 1800	
			du Pont	1 x 1800	
15ep	08 21 06.2	-72 20 11.2	du Pont	6 x 1800	VI
15kl	16 06 14.8	-04 35 49.7	Magellan/Baade	2 x 300	VRI
15ll	22 40 02.7	+26 30 45.1	Magellan/Baade	4 x 1800	VRI
			LBT	2 x 4 x 1200	VRI
15oy	02 48 35.7	+19 16 26.6	Magellan/Baade	2 x 1000	VRI
15tv	01 35 11.7	+26 25 38.8	LBT	2 x 3 x 800	VRI
16cx	16 11 58.5	+54 56 42.9	LBT	2 x 2 x 1200	$\cdots$
16di	14 16 36.4	+01 52 05.7	Magellan/Baade	2 x 1200	VRI
16dj	10 07 17.7	+69 20 46.2	MDM	4 x 1200	VRI
16dr	12 27 04.2	+25 41 01.6	Magellan/Baade	3 x 1800	VRI
16du	07 53 11.6	+28 16 42.4	LBT	2 x 6 x 1200	VRI
16gt	10 37 02.4	-18 27 44.8	du Pont	2 x 1500	BVI
16hl	16 04 55.2	-72 23 18.3	du Pont	3 x 1500	VI
16hq	16 05 16.5	+00 07 05.5	Magellan/Baade	3 x 1200	VRI
16kq	08 09 33.9	+02 15 39.7	du Pont	4 x 1800 + 1 x 1500	BVI
GJ3039	00 32 34.9	+07 29 26.5	du Pont	2 x 300	V

Table 3. ASAS-SN Photometry of Flares

ASAS-SN	UT	V	
number	date	3σ limit	detection
13ba	2013-06-28.5679994	16.71	⋯
	2013-06-28.5693679	16.54	⋯
	2013-07-02.5574708	16.22	12.04±0.01
	2013-07-02.5588631	16.39	12.40±0.01
	2013-07-05.5604776	17.53	⋯
	2013-07-05.5618807	17.50	⋯
13be	2013-07-05.4018670	18.04	⋯
	2013-07-05.4032605	18.22	18.19±0.35
	2013-07-06.4012965	17.98	16.02±0.06
	2013-07-06.4026820	18.08	16.25±0.07
	2013-07-08.3802245	17.87	⋯

NOTE—Example table provided for guidance; full table available online.

scope at the Las Campanas Observatory (LCO). We used the Wide Field CCD in long slit grism mode yielding a wavelength range $370 - 910$ nm, and resolution 8Å. We obtained optical spectroscopy for faint southern sources using the Inamori-Magellan Areal Camera & Spectrograph (IMACS; Dressler et al. 2011) on the Baade-Magellan 6.5-m telescope. We observed candidates with the F/2 camera, 0.″7-0.″9 slits, 300 lines per mm grism at a blaze angle of 17.5 degrees yielding a wavelength range $390 - 800$ nm and a dispersion of $\sim$ 1.3 Å pixel^{-1}. Optical spectroscopy for bright northern sources was obtained using the the Ohio State Multi-Object Spectrograph (OSMOS; Martini et al. 2011) on the MDM Observatory Hiltner 2.4-m telescope. We observed candidates with 0.″9-1.″2 slits and VPH grism yielding a wavelength range $390 - 680$ nm and R∼ 1600.

We reduced the spectra from Magellan, du Pont, and MDM using standard IRAF routines, supplemented by cosmic ray removal using the LA cosmic detection algorithm (van Dokkum 2001). Wavelength calibration for Magellan and DuPont used arc lamps taken at the position of the observations and resulted in solutions good to 0.1–0.3 pixels. For MDM, arc lamps were typically taken once per night, resulting in

wavelength solutions good to 0.5 pixels with 1–4 pixel offsets that we corrected using the Hα emission line. No radial velocity standards were taken with any telescope, so measuring velocities from the spectra was not attempted. For all three telescopes, we performed flux calibration using observations of a single flux standard per night.

We obtained spectra for the faintest northern sources with the Multi-Object Double Spectrograph 1 (MODS1; Pogge et al. 2010) mounted on the dual 8.4-m Large Binocular Telescope (LBT) on Mt. Graham. The MODS data were reduced with a combination of the MOD-SCCDRED[3] PYTHON package and the MODSIDL pipeline[4]. The reductions included bias subtraction, flat-fielding, 1-D spectral extraction, wavelength calibration using an arc lamp, and flux calibration using a spectroscopic standard taken the same night.

We assigned optical spectral types to each star based on comparison to the Bochanski et al. (2007) SDSS spectroscopic templates. Of the 53 stars, 47 were classified as M dwarfs with types M2–M9, as listed in Table 1, along with one K5 dwarf (ASASSN-14he), one L0 dwarf (ASASSN-16ae; Schmidt et al. 2016). Spectral classifications for the stars are given in Table 1, and photometry for the other objects is given in Table 4. We include the L0 dwarf in our statistics and results because its chromospheric activity is not expected to be distinct from that of the 10 M7–M9 dwarfs included in the sample. We exclude the K5 dwarf because it is significantly more massive than the rest of the sample (types M2 and later).

In addition to these ASAS-SN flare stars, we also observed one previously identified TT Tauri star (see Section 6.3) and one newly identified young star (see Section 6.5). For one faint ob-

---

[3] http://www.astronomy.ohio-state.edu/MODS/Software/mod
[4] http://www.astronomy.ohio-state.edu/MODS/Software/mod

ject, ASASSN-14aa, the spectrum of a $V = 23.4$ mag source close to the ASAS-SN position is not stellar, and upon further examination the real source of the outburst is likely to be a $V = 25.2$ mag point source nearby. Follow-up Magellan photometric observations of another faint source, ASASSN-14be, was unable to identify any source consistent with the ASAS-SN position. We place 5-sigma limits of $V > 25.6$, $R > 24.9$, and $I > 23.6$ mag at the position of ASASSN-14be, making its counterpart significantly too faint to obtain a spectrum of sufficient quality to provide a spectral type. Because the stellar photometry meets color selection criteria for M dwarfs, ASASSN-14aa and ASASSN-14be are likely to be $\Delta V < -10$ mag flares on distant M dwarfs. We do not include them in this analysis due to the lack of spectroscopic observations.

4. CALCULATING FLARE ENERGIES

The magnitudes for each observation of the 55 flares detected on 49 objects are given in Table 3. Each ASAS-SN flare detection includes between one and six individual observations. Most of these observations span $\sim$2–8 minutes, with only three flares (including ASASSN-13cb; Schmidt et al. 2014) having additional ASAS-SN detections within less than a day. Typically, there are non-detections or detections at the quiescent (non-flaring) magnitude $\sim$24–48 hours before and after the event, but these data points do not provide useful constraints on flares, which typically last 1–6 hours (Davenport et al. 2014b). To examine the data from each flare, we first convert both the quiescent and flaring V-band magnitudes to V-band fluxes, then subtract the quiescent flux from all flare data to obtain flare-only fluxes.

Distance is an essential factor in converting flare fluxes to energies. We obtained distances (given in Table 5) for 42 of the 49 stars via a cross-match to the Bailer-Jones et al. (2018) catalog of distances derived from Gaia DR2 parallaxes (Gaia Collaboration et al. 2018; Lindegren et al. 2018). These Gaia distances have uncertainties of 1% for the brighter ($V < 19$) stars and closer to 7% for the fainter stars. The remaining 7 stars include the nearby binary star GJ3039, the four faintest M dwarfs, and two stars that have poor astrometric solutions due to nearby background objects. We calculated distances for the remaining stars in our sample using available photometry. For four of the dwarfs, we combined our V-band photometry with 2MASS K_S-band to use the $V - K_S$ relation from Henry et al. (2004). For the three dwarfs without reliable K_S or Gaia matches, we used high quality SDSS photometry to calculate distances. For the faint early-M dwarfs ASASSN-13dj and ASASSN-15ll, we used the $r - z$ relation from Bochanski et al. (2011) to derive distances and for the L0 ASASSN-16ae, we used the $i - z$ relation from Schmidt (2018, in prep.). The photometric distances have a mean uncertainty of 18%. Because we examined only the brightest flares, the ASAS-SN flare sample is biased towards nearby objects; the majority (43 of 49 objects) are located within 200 pc, with five additional objects between 200 and 400 pc, and only ASASSN-13dj and ASAS-SN15ll (1090 ± 220 pc and 1000 ± 190 pc, respectively) found at larger distances.

4.1. Lower Limits on V-band Flare Energies

The survey strategy of ASAS-SN—acquiring two or three 90 second dithers on a field before moving on to another field—does not allow for a detailed analysis of flare lightcurves, but the data are sufficient to place accurate lower limits on the V-band flare energy. Given a single detection that indicates a flare-type brightening, the lowest energy flare that could correspond to that observation is a simple, classical flare with the peak of the flare occurring during that single observed point. We calculate the flare energy based on the fit of a simple, classical flare to the data and refer to it as a lower-limit be-

Table 4. M dwarf Contaminants

ASAS-SN	other	Photometry				
number	designation	J	H	K_S	$W1$	$W2$
ASASSN-15af	2MASS J01575499-5430367	15.13±0.04	14.63±0.04	14.27±0.06	14.15±0.03	13.92±0.03
ASASSN-16hl	2MASS J16045515-7223199	14.14±0.03	13.43±0.03	13.30±0.04	12.92±0.03	12.81±0.03

cause other light-curves that fit the points have a higher energy (see Section 4.4.1).

For the simple, classical flare, we draw on the Davenport et al. (2014b) empirical flare template, which parameterizes the flare as a fast rise phase

$$\frac{F_{\rm rise}}{F_{\rm amp}} = 1+1.941t_{1/2}-0.175t_{1/2}^2-2.246t_{1/2}^3-1.125t_{1/2}^4 \tag{1}$$

and a two-component exponential decay phase

$$\frac{F_{\rm decay}}{F_{\rm amp}} = 0.689e^{-1.600t_{1/2}} + 0.303e^{-0.278t_{1/2}}. \tag{2}$$

The flare is entirely characterized by the flare amplitude ($F_{\rm amp}$) and the half-light decay timescale ($t_{1/2}$). Davenport et al. (2014b) created this flare template from the co-added lightcurves of the 885 simple, classical flares found in *Kepler* data for M4 GJ 1243, the most active M dwarf in the original *Kepler* field. In addition to $F_{\rm amp}$ and $t_{1/2}$, the agreement between the flare template and the flare observations depends sensitively on the position of the template peak relative to the integration times of the observed data point. Because we are calculating the lower limit on the V-band flare energy, we assume that the actual flare peak occurred during the ASAS-SN observations, and let the exact position of the template peak vary between the times of the first and last observed data points.

To estimate the best fit of the flare template to the observations, we first generated 400 flare light curves with $t_{1/2}$ varying from 10 to 2000 s in increments of 5 s. We integrated the flare lightcurve over the exposure time for each data point (90 s), varying the position of the peak from the beginning of the first exposure to the end of the last exposure in increments of 1 s. For each combination of peak position and $t_{1/2}$ we compared the integrated fluxes to the data points, accepting the parameters where the normalized integrated light-curve fell within the 1-σ uncertainties of the observed fluxes.

The parameter space where the flare template and observations are in agreement is not distributed normally with respect to $t_{1/2}$ or peak position, so we adopt the median values as the best fit result and the interquartile range as the asymmetric uncertainties. We obtain the V-band energy released from the best-fit flare template by integrating over total flare time, and multiplying by the distance factor (d^2) and V-band central wavelength (5500 Å). The resulting V-band energy is then a lower limit of the observed ASAS-SN flare. These lower limits on the V-band energy range from $\log(E_V/{\rm ergs}) = 32$ to 35 are shown as a function of spectral type in Figure 1 and listed in Table 6.

We examined the observations and the range of best-fit template curves for each flare to classify each set of data points as occurring during the rise or decay phase of each flare. We found that of the 54 flares with more than one photometric observation, we observed the rise phase 16 times, the decay phase 37 times, and we caught the peak in the middle of three observations for one flare. Over the course of an entire flare, the decay phase is roughly 12 times longer than the rise phase (Davenport et al. 2014b). It is unlikely that we are observing the end of the decay phase, however, since flares are much

Table 5. Kinematics

ASAS-SN number	kinematics source	d [pc]	z [pc]	$\mu_\alpha \cos(\delta)$ [mas/yr]	μ_δ [mas/yr]	$V_{\tan}$ km s^{-1}
13ba	Gaia	113.4±2.1	−89.4	154.8±0.3	67.7±0.1	91.4±1.7
13be	Gaia	127.1±1.3	73.1	−131.7±0.1	−142.1±0.2	117.5±1.2
13bf	Gaia	339.5±9.6	−278.2	−16.3±0.1	−25.7±0.1	49.2±1.4
13bg	Gaia	52.9±0.4	−27.3	23.2±0.2	97.6±0.1	25.3±0.2
13bh	Gaia	144.4±2.4	−83.8	−9.9±0.2	3.7±0.2	7.3±0.2
13bi	Gaia	106.3±0.9	97.7	8.0±0.1	−21.7±0.1	11.7±0.1
13bk	Gaia	183.4±3.1	116.5	−16.3±0.2	29.9±0.2	29.8±0.6
13bl	Gaia	43.9±0.1	36.6	11.5±0.1	51.5±0.1	11.1±0.0
13bn	Gaia	177.5±3.8	−55.8	−11.2±0.1	9.8±0.1	12.6±0.3
13bt	Gaia	171.7±18.8	144.7	−45.6±1.1	44.9±1.4	52.4±5.9
13cb	Gaia	75.6±2.9	−31.9	125.9±1.0	−22.6±0.9	46.2±1.9
13cm	Gaia	59.1±0.2	−41.7	54.0±0.1	16.6±0.1	15.9±0.1
13cr	Gaia	112.1±5.0	−42.6	29.6±0.7	−20.6±0.4	19.3±1.0
13de	Gaia	151.1±2.1	−75.0	1.0±0.1	−9.1±0.1	6.6±0.1
13di	Gaia	381.8±32.4	187.6	−3.2±0.3	−0.9±0.3	6.0±0.9
13dj	r-z/2M-W	1086.7±217.0	−749.1	· · ·	· · ·	· · ·
13dk	V-K/2M-W	189.9±34.7	154.6	29.2±7.7	−20.6±5.5	32.4±10.4
14bj	Gaia	185.3±6.7	176.7	−8.3±0.4	−44.0±0.3	39.6±1.5
14bm	Gaia	263.8±24.2	237.4	−5.8±0.7	−10.1±0.6	14.7±1.8
14bn	Gaia	83.0±0.6	−67.3	−76.9±0.2	−6.6±0.1	30.5±0.2
14cx	Gaia	136.8±2.7	60.5	5.4±0.2	−6.6±0.3	5.5±0.2
14dv	Gaia	176.6±11.7	−156.6	54.1±0.6	20.5±0.4	48.8±3.3
14ea	Gaia	56.5±0.3	−21.5	63.8±0.1	−54.8±0.1	22.7±0.1
14fi	Gaia	123.5±0.8	−77.0	16.2±0.1	23.7±0.1	16.9±0.1
14gj	Gaia	193.3±14.7	−72.2	−14.9±0.8	−10.8±0.6	17.0±1.6
14gn	Gaia	199.8±17.1	−94.7	−34.7±0.8	−24.6±0.6	40.5±3.6
14hc	Gaia	111.3±1.9	−50.9	−35.9±0.3	−7.3±0.1	19.4±0.4
14hz	Gaia	186.3±11.0	−98.4	18.4±0.5	5.4±0.4	17.0±1.2
14ji	Gaia	175.4±20.1	−101.7	−10.3±0.9	−45.3±0.7	38.9±4.6
14jw	Gaia	47.9±0.4	−21.7	−198.4±0.3	−126.3±0.4	53.8±0.5
14jy	Gaia	46.3±0.1	−2.4	−4.8±0.1	−39.1±0.1	8.7±0.0
14ke	Gaia	142.6±24.7	−87.8	60.7±1.1	−13.3±0.9	42.3±7.4
14lc	V-K/2M-W	91.3±17.4	104.5	51.0±15.3	13.9±7.1	23.0±8.5
14mz	V-K/2M-W	74.4±13.5	57.5	68.9±3.7	−9.9±7.8	24.7±5.4
15ep	Gaia	159.3±3.7	−37.9	−17.0±0.2	41.9±0.3	34.4±0.8
15kl	Gaia	65.8±0.5	51.0	74.5±0.2	−44.1±0.1	27.2±0.2
15ll	r-z/2M-W	999.1±185.5	−450.1	· · ·	· · ·	· · ·
15oy	Gaia	24.9±0.1	0.5	248.4±0.2	−124.7±0.2	33.1±0.1
15tv	Gaia	148.3±4.2	−70.8	36.2±0.4	−14.1±0.3	27.5±0.8
16ae	i-z/2M-W	77.9±14.0	−7.8	126.5±11.7	157.3±26.3	75.0±17.2
16cx	Gaia	79.7±2.8	70.9	−20.4±1.2	75.3±0.8	29.6±1.2
16di	Gaia	137.2±10.6	130.7	−10.9±1.0	−19.2±0.7	14.4±1.4
16dj	Gaia	52.5±0.1	49.9	−18.1±0.1	23.1±0.1	7.3±0.0
16dr	Gaia	100.0±4.0	114.5	−13.6±0.4	−5.9±1.1	7.1±0.6
16du	Gaia	237.6±48.5	116.3	−2.1±1.2	−24.9±0.6	28.3±6.0
16gt	Gaia	28.5±0.1	30.9	−421.1±0.1	−25.5±0.1	57.3±0.2
16hq	Gaia	108.7±5.4	79.1	−51.9±0.8	−14.6±0.6	28.0±1.5
16kq	Gaia	107.0±1.5	48.9	−55.7±0.2	11.2±0.1	29.0±0.4
GJ3039	V-K/2M-W	10.6±1.9	6.3	−95.7±7.3	75.5±3.5	6.2±1.2

fainter then. The ratio of decay phase to rise phase observed for the ASAS-SN sample (2.31) corresponds to the ratio of decay phase to rise phase for the flare template if it is only visible at 52% or more of its peak value. Hence, the balance of observations occurring during rise versus decay is a good indicator that we are likely observing most flares close to their peak values.

4.2. *Flare Timescales*

The timescales for each flare are determined from one or two points. To test whether the resulting flare timescales are reasonable, we compare to the correlations between flare energy and flare length found in high cadence M dwarf observations from *Kepler* data (Hawley et al. 2014; Silverberg et al. 2016). They derive two linear relationships, one for classical flares and one for multi-peaked complex flares. We convert the relationship between flare duration and *Kepler*-band energy to $t_{1/2}$ and V-band energy assuming $t_{1/2} = 0.14 \times t_{\mathrm{duration}}$ (Davenport 2016) and a flare SED of a 10,000 K blackbody (see, e.g., Kowalski et al. 2013) to convert energies between the two bands ($E_{Kepler} = 1.9E_V$). Figure 2 shows the relationship between timescale and flare energy compared to the timescales and energies derived from the fitting procedure described in the previous section. We also calculate energies for each flare based on that relationship; because flare energy and $t_{1/2}$ are dependent on each other, we calculate them iteratively until the change in the log of energy is less than 0.01 between steps. The final values (given in Table 6) fall within an order of magnitude of those based on the fitting procedure, and are on average a few percent stronger.

Compared to the relationship from *Kepler* data, approximately half of the flares have timescales and energies that are in the expected range based on the *Kepler* flare data, but the remaining half have shorter timescales than expected for flares with their peak flux. The majority of the ASAS-SN flares are higher energy

than those observed in *Kepler* data of GJ 1243, however, so the relationship between duration and energy has been extrapolated to higher energies than it may be applicable. In a sample of ~ 20 well-characterized flares, Kowalski et al. (2013) found that larger flares were more impulsive (shorter $t_{1/2}$) than smaller flares, indicating the relationship between duration and energy may be shallower at higher flare energies. The relationship between half-light timescale ($t_{1/2}$) and total duration is also based on a single flare peak, and so does not hold for complex flares that have multiple peaks. Complex flares would have shorter measured $t_{1/2}$ than the expected values for simple flares. Each of these factors lead to an underestimate of the total flare energy, so the V-band energies derived from the light-curve fits are conservative as lower limits.

4.3. *Flares With Extra Observations*

Three of the ASAS-SN flare M dwarfs had additional observations from the same flare separated by more than a few minutes, and we examine these to better understand the limitations of our fit. For ASASAN-13bg and ASASSN-14jy, this occurred because the stars are positioned on the overlap strip between two different ASAS-SN fields, resulting in two sets of observations separated by ~ 15 minutes. For ASASSN-13cb, the additional observations were an effort to obtain follow-up data for this dramatic transient event (see Schmidt et al. 2014). During our fitting procedure, we excluded points farther than 1000 s from the peak to focus on the data from a singe telescope pointing, so the fits for those three objects are based on a subset of the available data. The light curves and fits for these objects are shown in Figure 3.

The best fit to ASASSN-13bg is based on two observations at the end of the rise phase of the flare, and there are two additional observations taken before the peak of the flare that fall above the model. To fit the later observations would require a longer $t_{1/2}$ than the

Table 6. Flare Properties

| ASAS-SN number	quiescent V	flare peak V	ΔV	flare type	# flare obs	fit $t_{\rm half}$ [s]	$log(E_V)$ [log(erg)] IQ 1	median	IQ 3	from $t_{\rm half}$ relation $t_{\rm half}$ [s]	$log(E_V)$ [log(erg)]
13ba	17.42±0.01	12.04±0.01	−5.38±0.01	decay	2	309	34.33	34.43	34.47	1927	35.14
13be	18.40±0.01	16.02±0.06	−2.38±0.06	decay	2	509	32.95	33.04	33.13	573	33.09
13bf	17.22±0.01	14.33±0.03	−2.89±0.03	rise	2	443	34.45	34.58	34.65	1942	35.15
13bg	17.13±0.01	14.82±0.04	−2.31±0.04	rise	4	1373	33.07	33.21	33.28	458	32.71
13bh	16.71±0.05	13.94±0.02	−2.76±0.05	decay	2	282	33.71	33.81	33.85	1217	34.36
13bi	18.08±0.01	14.81±0.03	−3.27±0.04	rise	2	1261	33.66	33.83	33.92	760	33.57
13bk	18.68±0.01	15.11±0.07	−3.57±0.07	single	1	⋯	⋯	⋯	⋯	1008	34.04
13bl	14.83±0.01	13.17±0.01	−1.66±0.02	decay	2	972	33.40	33.50	33.55	650	33.30
13bn	17.16±0.02	15.08±0.06	−2.08±0.06	rise	2	1315	33.97	34.13	34.21	953	33.95
13bt	19.14±0.06	14.62±0.03	−4.52±0.07	rise	2	236	33.50	33.63	33.74	1132	34.24
13cb	21.97±0.15	12.85±0.01	−9.13±0.15	decay	7	270	33.61	33.70	33.75	1137	34.25
13cm	16.21±0.03	13.43±0.02	−2.78±0.04	decay	4	545	33.39	33.49	33.54	777	33.60
13cr	14.82±0.02	12.41±0.01	−2.41±0.02	rise	2	1471	34.73	34.86	34.92	1640	34.86
13de	18.14±0.02	15.38±0.05	−2.76±0.06	rise	2	877	33.59	33.71	33.78	799	33.65
13di	19.97±0.06	16.00±0.11	−3.97±0.12	rise	2	1283	34.32	34.46	34.54	1262	34.42
13dj	23.09±0.04	17.35±0.23	−5.74±0.24	decay	2	1188	34.60	34.80	34.90	1702	34.93
13dk	19.91±0.02	15.81±0.11	−4.10±0.11	rise	2	562	33.45	33.58	33.66	833	33.72
14bj	19.73±0.01	16.71±0.13	−3.02±0.13	rise	2	838	33.18	33.31	33.42	608	33.19
14bm	20.47±0.01	16.10±0.09	−4.37±0.09	decay	2	1245	33.94	34.08	34.19	953	33.95
14bn	17.40±0.04	14.46±0.04	−2.94±0.05	decay	2	290	33.03	33.13	33.18	711	33.45
14cx	19.62±0.02	14.33±0.03	−5.29±0.04	decay	2	1254	34.11	34.21	34.30	1065	34.13
14dv	20.72±0.01	14.67±0.06	−6.05±0.06	decay	2	614	33.88	33.99	34.09	1143	34.25
14ea	15.78±0.01	13.77±0.02	−2.01±0.02	decay	2	360	33.02	33.12	33.16	658	33.32
		14.69±0.04	−1.09±0.05	decay	2	336	32.49	32.59	32.65	447	32.67
14fi	17.21±0.03	13.58±0.03	−3.63±0.04	rise	2	1317	34.34	34.45	34.51	1245	34.40
14gj	20.63±0.05	15.68±0.06	−4.95±0.08	decay	2	355	33.37	33.46	33.53	882	33.82
14gn	21.38±0.04	15.80±0.25	−5.58±0.25	rise	2	1061	33.66	33.83	33.97	871	33.79
		15.88±0.08	−5.50±0.09	rise	2	637	33.53	33.65	33.73	848	33.75
14hc	18.99±0.02	14.10±0.04	−4.89±0.04	decay	2	181	33.29	33.39	33.44	993	34.02
14hz	20.16±0.02	15.42±0.06	−4.74±0.06	decay	2	699	33.67	33.78	33.89	932	33.91
14ji	22.42±0.05	16.92±0.23	−5.50±0.23	rise	3	1260	33.24	33.34	33.43	559	33.05
		16.19±0.13	−6.23±0.14	decay	2	76	32.54	32.64	32.72	703	33.43
14jw	18.96±0.06	14.54±0.04	−4.42±0.07	decay	2	981	32.98	33.10	33.20	485	32.81
14jy	15.05±0.01	12.10±0.01	−2.95±0.01	decay	2	1421	34.09	34.21	34.28	1005	34.04
		12.05±0.01	−3.00±0.01	rise	2	379	33.57	33.70	33.78	1020	34.06
		13.72±0.02	−1.33±0.02	rise	4	1321	33.28	33.42	33.51	548	33.02
14ke	21.03±0.04	15.29±0.06	−5.74±0.07	decay	2	143	32.95	33.04	33.10	811	33.67
14lc	24.20±0.10	14.86±0.07	−9.34±0.12	decay	2	97	32.61	32.70	32.76	686	33.39
14mz	19.38±0.02	13.17±0.01	−6.21±0.02	decay	2	548	33.74	33.84	33.88	1016	34.05
		16.89±0.28	−2.49±0.28	middle	3	1078	32.32	32.51	32.64	303	32.03
15ep	19.66±0.03	15.68±0.16	−3.98±0.16	decay	2	1177	33.59	33.77	33.89	767	33.58
15kl	17.21±0.04	14.64±0.05	−2.57±0.06	decay	2	909	33.16	33.27	33.37	569	33.08
15ll	22.60±0.03	14.89±0.04	−7.71±0.05	decay	2	151	34.82	34.92	34.97	3493	36.15
15oy	18.63±0.01	13.92±0.04	−4.71±0.04	decay	3	1401	32.88	32.93	32.97	378	32.39
15tv	19.66±0.01	13.61±0.02	−6.05±0.02	decay	3	341	34.02	34.04	34.05	1415	34.61
16ae	23.75±0.34	13.51±0.02	−10.24±0.34	decay	3	595	33.51	33.67	33.80	942	33.93
16cx	22.81±0.18	15.01±0.04	−7.80±0.19	decay	3	1082	33.34	33.39	33.45	597	33.16
16di	20.36±0.01	15.79±0.07	−4.57±0.07	decay	6	1533	33.67	33.74	33.79	672	33.36
16dj	16.03±0.01	12.29±0.01	−3.74±0.01	decay	3	668	33.90	33.92	33.93	1045	34.10
16dr	19.60±0.02	13.87±0.02	−5.73±0.03	decay	3	1157	33.87	34.06	34.18	996	34.02
16du	21.80±0.07	16.17±0.14	−5.63±0.16	decay	3	1222	33.78	33.93	34.03	871	33.79
16gt	17.09±0.02	12.69±0.01	−4.40±0.02	decay	3	253	32.90	32.91	32.92	609	33.19
16hq	21.55±0.02	13.35±0.02	−8.20±0.03	decay	3	469	33.98	34.00	34.01	1242	34.39
16kq	18.17±0.01	14.56±0.04	−3.61±0.04	decay	3	1096	33.64	33.82	33.95	829	33.71
GJ3039	12.66±0.01	11.66±0.01	−1.00±0.01	decay	2	1142	32.73	32.82	32.87	362	32.33
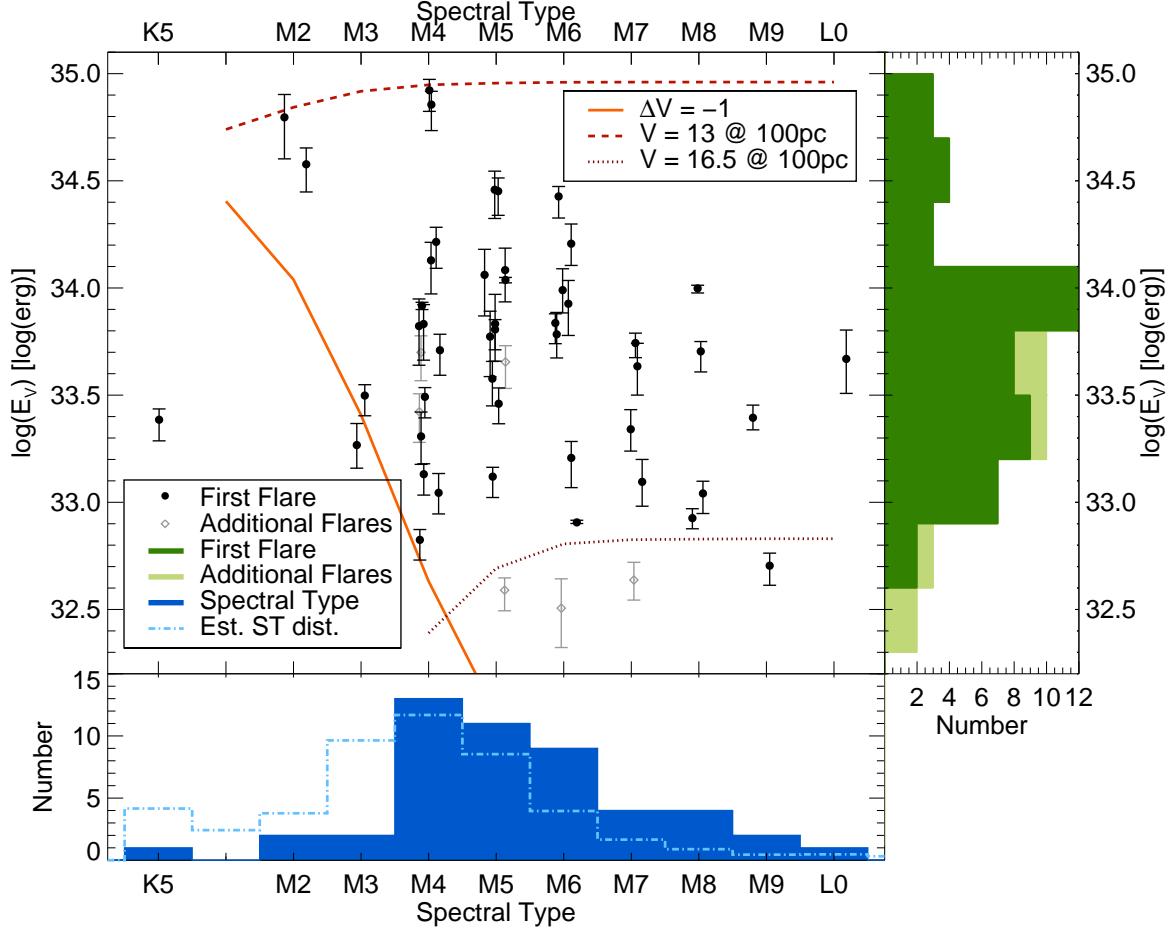
Figure 1. The log of the lower limit on V-band energy ($\log(E_V)$) as a function of spectral type. The lower energy flares from M dwarfs with multiple flares (grey points; light green histogram) are distinguished from the main sample of flares (black points, dark green histogram). The lower limit V-band energies range from $\log(E_V/\mathrm{ergs}) = 32$ to 35, and are set by the detection limit of ASAS-SN ($\sim V < 16.5$ mag, as shown in the red dashed lines). The spectral type distribution (dark blue) is comparable to a distribution drawn from the Bochanski et al. (2011) M dwarf luminosity function (light blue dot dashed line) where M3 and earlier dwarfs are under-represented due to the ASAS-SN detection limits. The lack of flares in the bottom left corner is an observational effect; these flares would likely be smaller than $\Delta V = -1.0$ (as shown by the orange line) and so unlikely to be found in the ASAS-SN search.
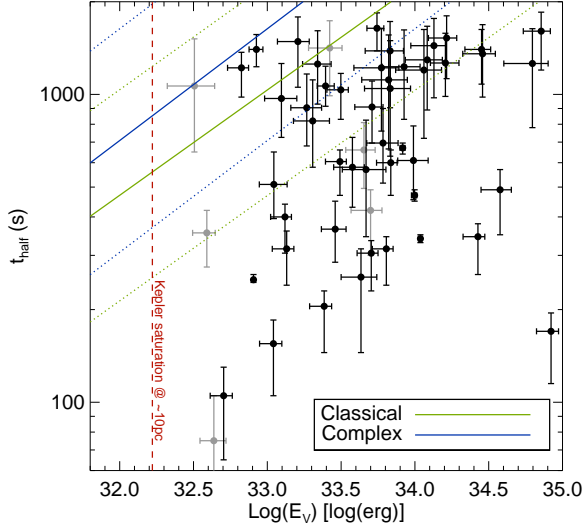
Figure 2. Flare timescale ($t_{1/2}$) as a function of the log of the best fit V-band energy. The ASAS-SN M-dwarf flares are compared to estimates of flare timescale based on the correlation between total flare duration and *Kepler* flare energy from Hawley et al. (2014) and Silverberg et al. (2016), shown for both classical (green) and complex (blue) flares. For each relationship, an order of magnitude spread in energy is shown (dotted lines) to demonstrate the range observed in flare data. A characteristic saturation limit for *Kepler* observations of flares on M dwarfs at 10pc is shown, based on the saturated data from GJ 1243 (red dashed line). The majority of *Kepler* flares analyzed in detail have energies below this line, so the relationships shown are extrapolations for energies greater than $\log(E_V/\text{ergs}) > 32.2$.

model shown, but the current best fit parameters already have a long half-light timescale ($t_{1/2} = 1373$ s) compared to the V-band energy ($\log(E_V/\text{ergs}) = 32.7$). Because they fall so far from the best fit to the peak observations, it is more likely that the points excluded from the fit are part of a different peak in the same flare. While the precursor peak could be very strong, a minimum fit to it would also be nearly an order of magnitude less energetic than the main flare and only contribute an additional few percent to the total energy.
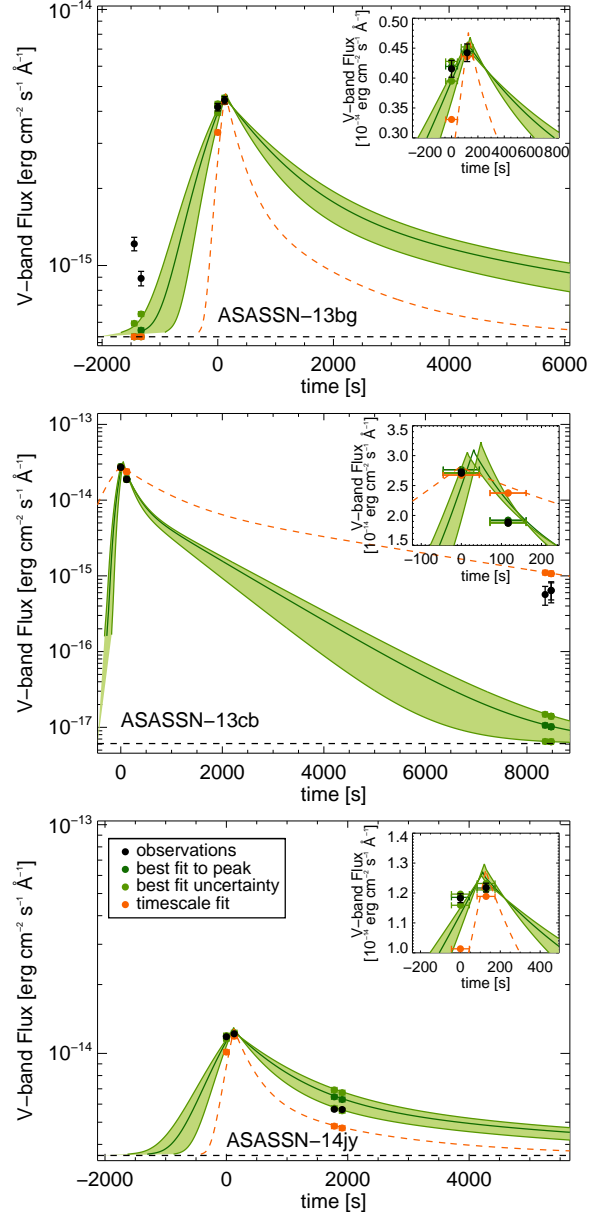
Figure 3. V-band flare flux from ASASSN-13bg (top), ASASSN-13cb (middle), and ASASSN-14jy (bottom) as a function of time, with the inset showing the same data near the peak of the flare. The flare observations are shown (black points with uncertainties) as well as the quiescent flux value (black dashed line). The best-fit flare template is shown (dark green line and points) with its uncertainties (light green shaded area), as well as a flare template based on the relationship between total energy and timescale from *Kepler* data (orange line and points; see Section 4.2). The data points generated from these each of these light-curves integrated over a 90 s exposure time are also shown. For 13cb and 14jy, the data points far from the peak do not fall near the best-fit curve, but for 14jy they do.

The best fit to ASASSN-13cb is based only on the two observations near the peak, not including two additional observations taken over two hours later. This resulted in a relatively short half-light timescale ($t_{1/2} = 270$ s) and a V-band energy ($\log(E_V/\mathrm{ergs}) = 32.7$) much lower than the original estimate from Schmidt et al. (2014), which included all points but did not have an empirical model for the flare. The timescale calculated from the *Kepler* relationship between energy and timescale ($t_{1/2} = 2563$ s) is an excellent fit to the later data points, however, and corresponds to a much higher energy ($\log(E_V/\mathrm{ergs}) = 34.4$). That timescale is a poor fit for the steep drop between the first two data points.

The match between the best-fit flare template and the observations is much better for ASASSN-14jy, with the points not included in the initial fit falling along the curve representing the lower quartile in uncertainty. This could indicate that the simple flare model is a good fit to at least some of the flares, but additional complexity could have occurred between the detected points.

Given that none of the data points for any of these three flares fall significantly below the best-fit lines, it is reasonable to continue to assume that the fits represent solid lower limits on the V-band flare energies.

4.4. *Upper Limits on Flare Energies*

While sparse observations can place a strong lower limit on flare energies, the upper limits of the observed flares are less clear. We examine possible upper limits from two different perspectives. First, we examine the variations in flare shape that would also fit the data in the context of previous work. Second, we use flare frequency distributions to estimate the probability of more luminous flares.

4.4.1. *Constraints on the Flare Shape*

In our energy estimates, we used the highest photometric observation as the peak of a classical flare template. We argue that these assumptions lead are both more likely to lead to a lower estimate of the flare energy, and so are valid lower limits. In Figure 4, we use ASASSN-14gj as a reference to demonstrate some possible higher-energy templates. One of the simplest higher-energy flare templates is a classical shape with an earlier peak at a higher flux. We show a flare with a peak at 10 times the observed peak flux, with a decay timescale of 107 s and a total energy of $E_V = 5.8 \times 10^{33}$ erg. The timescale is very short for this template due to the strong difference between the first two points, and would fall well below the relationship shown in Figure 2. The combination of timescale and energy is unlikely to be physically possible because the volume of hot plasma needed to produce the peak luminosity cannot cool that quickly. Thus, assuming a classical flare template and the observed decay between dithered observations, it is likely that we discovered ASASSN-14gj near its peak. Because the timescales of the majority of ASAS-SN flares are already low compared to their energies, a similar argument can be made for the majority of the flares observed.

While it seems likely that most of these flares were observed near their peak, the assumption that all these flares are simple, classical flares is less likely to be true. Davenport et al. (2014b) find that approximately 15% of the flares detected on GJ 1243 are complex, multi-peaked events. Hawley et al. (2014) and Silverberg et al. (2016) found that the fraction of complex flares increases with flare energy, with around half of flares above 10^{33} ergs typically showing complex behavior. The higher incidence of complex events at high energies is, in part, because very energetic flares cover a relatively large area of the stellar surface and are more likely to trigger sympathetic flaring (e.g.,
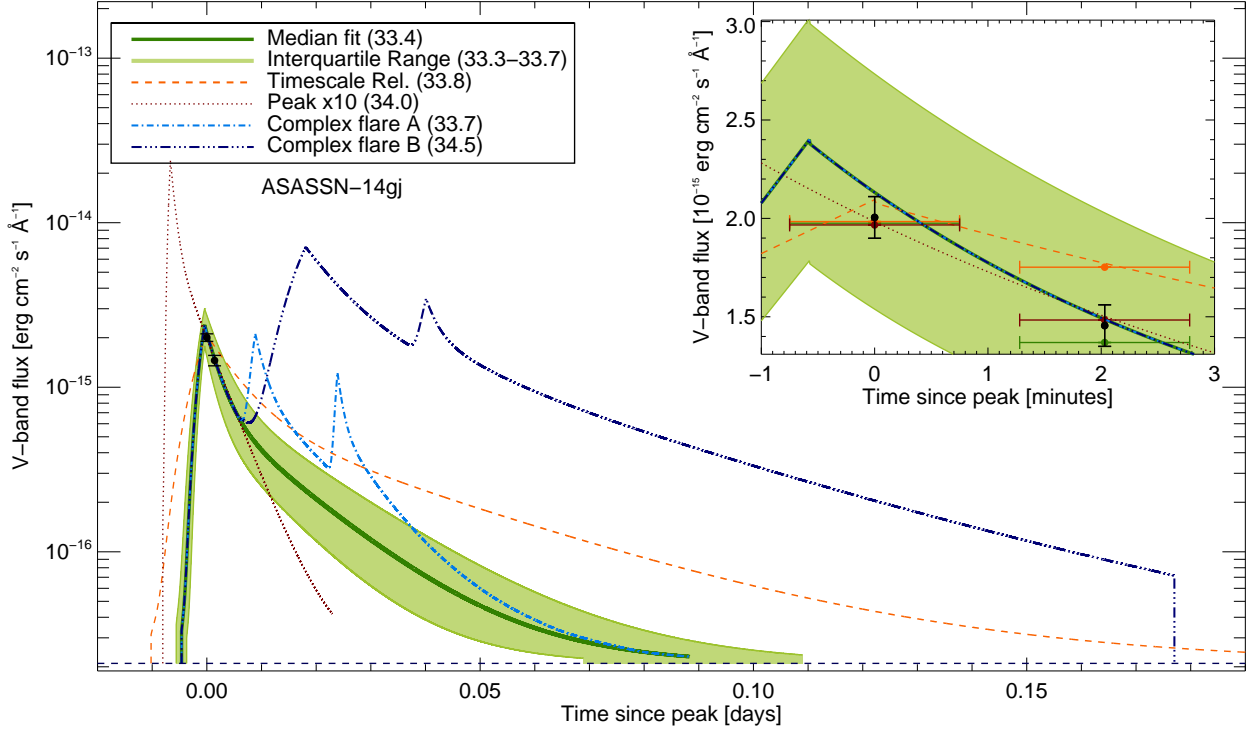
Figure 4. *V*-band flare flux from ASASSN-14gj as a function of time over 0.2 days, with an inset showing flare flux as a function of time over 4 minutes. The flare data is shown (black points with uncertainties) as well as the quiescent value (black dashed line). For each example flare shown, the full lightcurve is plotted (lines) along with the fluxes integrated over the exposure time of the data (90 s; points with horizontal error bars). The flare timescale fit to the data is shown (dark green line) with its uncertainties (light green shaded area), as well as a flare calculated to fall along the relationship between flare energy and duration found from *Kepler* data for GJ 1243 (orange dashed line; Hawley et al. 2014; Silverberg et al. 2016). A light curve with a peak at 10 times the observed peak is shown (red dotted lines), and two possible complex flares with multiple peaks are shown (dot dashed light blue and triple-dot dashed dark blue). For reference the log of the *V*-band energies under each of these curves is given in the legend.

Anfinogentov et al. 2013). Because the ASAS-SN flares are mostly higher energy than 10^{33} erg, nearly half of the 55 flares are probably complex and so would be poorly fit by the empirical classical flare template. Figure 4 shows two of many possibilities for complex, multi-peaked events, drawing inspiration from previously observed M dwarf flares (Hawley & Pettersen 1991; Kowalski et al. 2013). It is not currently possible to estimate the presence or strength of multiple peaks based on sparse observations near the peak, but since the addition of more peaks increases the energy, the classical flare as-

sumption continues to be a conservative lower limit.

4.4.2. *The Frequency of Larger Flares*

While the high occurrence rate of complex flares presents difficulties for placing an upper limit on a flare given a very sparse light curve, the distribution of flares at each energy is relatively well understood and can be used to place limits on flare energy. Lacy et al. (1976) first related the occurrence of flares to their energy, finding that on a handful of M-dwarfs, a flare that releases an order of magnitude more energy may occur ten to one-hundred times less

frequently than smaller flares. This flare frequency distribution (FFD) has been observed and quantified for a number of stars, typically characterized by a power-law slope ranging from -0.5 to -1.3, dependent on spectral type and activity level. While our work eventually aims to quantify the FFD of M dwarfs, we can use previous results to examine the occurrence of large flares.

To place some upper limits on flare frequency, we use the upper and lower bounds of α, the power law slope, from Hilton (2011); Hawley et al. (2014), to calculate a cumulative probability distribution of a given M-dwarf flare. If we assume no observational bias against flares of any size, each flare observed is increasingly less likely to be larger, proportional to their overall frequency. For example, the ASASSN-14gj flare with a lower limit of $\log(E) = 33.5$ is 92% likely to have an energy of less than 34.5, and 99% likely to have an energy less than 35.5. Given the spread expected from the energy uncertainty and the range of possible α values, the flare is $>70\%$ likely to be within an order of magnitude of the original estimate, and $>97\%$ likely to be within two orders of magnitude.

4.5. The Distribution of Flares and Stars

The energies of flares and distribution of spectral types is essentially a scatter plot, with the shape of the distribution being set primarily by the underlying stellar population and the observational constraints rather than a fundamental property of flares.

One limit on our detection of flares in early-M dwarfs is the contrast effect; on a dim, late-M dwarf, an energetic flare will have a much higher contrast with the underlying photosphere than it would on a bright, early-M dwarf. To show this effect, we calculated a characteristic energy for a one magnitude flare ($\Delta V = -1$) as a function of spectral type. To convert peak flux to energy, we used the relationship between flare

peak and flare energy discussed in Section 4.4.1. That limit (shown in Figure 1) falls below the majority of the flares for dwarfs earlier than M5. For dwarfs later than M5, flares smaller than $\log(E_V/\mathrm{ergs}) = 32$ would still have a contrast of greater than one magnitude. Due to the current classification methods of ASAS-SN, a flare of less than one magnitude is unlikely to have made it on our list.

We also examined the effect of the faint detection limit of ASAS-SN on the range of energies detected. The detection limit varies from night to night, but is typically above $V=16$ (and can be as faint as $V=17.5$). At a distance of 100 pc, that limit corresponds to a flare energy of $\log(E_V/\mathrm{ergs}) = 33$, and there are fewer flares than expected that fall below that energy. Those flares are likely to have occurred during good conditions or on more nearby stars.

To understand the distribution of spectral types, we calculated the distribution expected if the 49 M dwarfs were drawn evenly from the Solar neighborhood (shown in Figure 1; based on the mass functions of Cruz et al. 2007; Bochanski et al. 2010). Overall, there are fewer M3 and earlier dwarfs than expected, and more later types. This is reasonable, given that flares of the same energy are more difficult to detect on these bright M dwarfs.

5. ASAS-SN FLARE STARS AS A POPULATION

The majority of flare surveys are targeted at specific stars (often particularly active ones), with the goal of examining detailed light-curves or photometry. ASAS-SN has the advantage of an agnostic flare selection, detecting flares wherever they occur. We use kinematics and the presence and strength of Hα emission to assess the ASAS-SN flare stars as a population to determine if these flares occurred on typical field stars or on peculiarly young and active stars.

5.1. Kinematics of the ASAS-SN M dwarfs

Kinematics are often used as age indicators for populations of stars; young stars typically have cold orbits characterized by low velocities with respect to the Sun and positions near the Galactic plane, while older stars have warmer orbits and are more likely to have higher velocities and be located further from the Galactic plane. The majority (45 of 49 objects) of ASAS-SN flare stars are located within 200 pc of the Galactic plane, with only two M dwarfs (ASASSN-13dj and ASASSN-15ll) found at Galactic heights greater than 400 pc (in this case, both below the plane).

We adopted Gaia proper motions for the 42 stars with matches in the Gaia database. For five of the seven remaining stars (excluding ASASSN-13dj and ASASSN-15ll due to the lack of 2MASS detections) we calculated proper motions based on the difference between 2MASS and WISE coordinates. The Gaia and 2MASS/WISE proper motions are given in Table 5). We combined these proper motions with distances to calculate tangential velocities (V_{tan}) for 47 dwarfs, which are also given in Table 5. The overall mean tangential velocity is 29.8 km s^{-1}, with a standard deviation of 22.6 km s^{-1}. There is a single M dwarf with a velocity larger than 100 km s^{-1} (ASASSN-13be with V_{tan} = 117.5 km s^{-1}). If this outlier is removed, the mean tangential velocity is 27.9 km s^{-1}, with a standard deviation of 18.7 km s^{-1}.

Comparing these to the data from Faherty et al. (2009) indicates that the M dwarfs in the ASAS-SN M-dwarf sample are slightly younger than M dwarfs in the Solar neighborhood, implying ages younger than ~5 Gyr and likely membership in the thin disk population. But with a few dwarfs at high Galactic heights and fast V_{tan}, it is not likely that they are a universally young population, nor are they significantly younger than the Galactic disk.

5.2. *Activity of the ASAS-SN M dwarfs*

As a manifestation of strong magnetic fields, the flare rate of M dwarfs is frequently correlated with other indicators of magnetic activity (Kowalski et al. 2009; Hawley et al. 2014). Our spectroscopic observations include the region surrounding the Hα emission line, frequently used as an indicator of activity in these low-mass stars (Gizis et al. 2000; West et al. 2008). We measured Hα equivalent widths (EW) using a custom IDL code that adopts the wavelength ranges and method described by West et al. (2011). Of our 49 stars, only three (K dwarf ASASSN-14hc and two M dwarfs) had no detectable emission in the Hα line. Both of the M dwarfs had spectra with sufficiently high signal-to-noise that an emission line with an EW of ~0.75 Å would be detectable; they either have Hα in relatively weak emission, weak absorption, or an absence of the activity indicator.

The activity fraction as a function of spectral type is shown in Figure 5 compared to the activity fraction of a reference sample of field M and L dwarfs that was selected based on color and not activity level (the SDSS DR7 M dwarf sample and the BOSS Ultracool Dwarfs sample; West et al. 2011; Schmidt et al. 2015). The two M dwarfs without detected activity (13dj and 15ll) have spectral types of M2 and M4; at those spectral types, the mean activity fractions (~ 5% and ~ 15% respectively) are relatively low, so the overall activity fraction of the ASAS-SN flare sample still falls well above the active fraction for those spectral types. These two dwarfs also have two of the strongest flares, and are the two most distant M dwarfs. Given their strong flares, it is surprising that they are not Hα emitters, but it is possible they are slightly older M dwarfs that have a lower base level of activity and flare much more rarely.

The Hα line strength can also be used to quantify the activity level of M dwarfs. EWs measure the strength of the line compared to the surrounding (psuedo-)continuum, but because
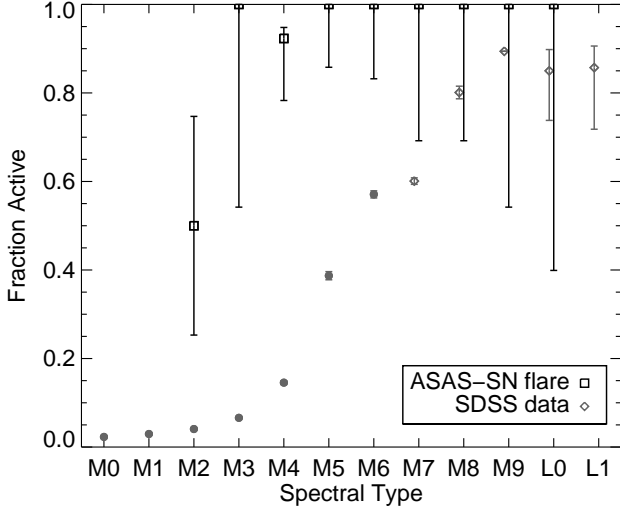
Figure 5. The fraction M dwarfs with activity (as defined by the presence of Hα emission) for the ASAS-SN flare dwarfs (black) compared to a sample selected based on colors (SDSS DR7 M dwarf and BUD ML dwarf samples; grey; West et al. 2011; Schmidt et al. 2015). The uncertainties are based on a binomial distribution. While the ASAS-SN flare sample is much smaller, it does also have a higher significantly active fraction than the comparison dwarfs.

the continuum varies with spectral type, we instead use the ratio of line luminosity to bolometric luminosity. We use the χ factor as a function of spectral type (West & Hawley 2008; Schmidt et al. 2014) to convert the EW to the ratio of Hα emission line flux to the stellar bolometric luminosity. Figure 6 shows the activity strength of the flaring ASAS-SN M dwarfs compared to that of the non-activity selected reference sample (West et al. 2011; Schmidt et al. 2015). We also show a parameterized activity strength, calculated by subtracting the median per spectral type from every value, then dividing by the difference between the 30% and 70% values. This parameterized activity strength is meant to aid comparisons of the ASAS-SN flare sample to the non-activity selected sample.

The majority (42 our of 48) of the M and L dwarfs fall at activity levels above the median
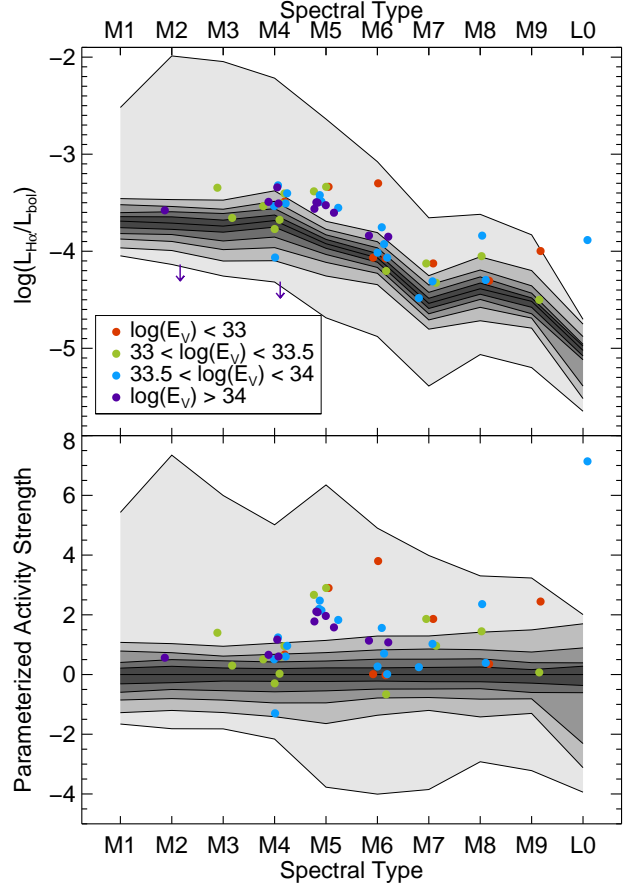
Figure 6. The log of the ratio of Hα line luminosity to bolometric luminosity (Hα activity strength) as a function of spectral type (top panel) and the parameterized activity strength (activity strength normalized so the median value is 0 and the interval between 30% and 70% is unity) as a function of spectral type (bottom panel) for the West et al. (2011) and Schmidt et al. (2015) M-dwarf samples compared to the activity strength and spectral type of the ASAS-SN flare sample. For the large M-dwarf samples, the shaded areas show percentiles in increments of 10%. For the ASAS-SN flare sample, the different total flare energy is indicated by each point's color.

value for their spectral types. Those that have less than the median activity level include the two inactive dwarfs, as well as a few more M4 and one M6 dwarf. There are 27 M dwarfs with activity strength that falls above the 90th percentile values for their spectral type. This indi-

cates that the ASAS-SN M dwarf flare sample is a significantly more active population than that of the field stars, consistent with previous results showing that stars without Hα emission flare less often than those with (Hawley et al. 2014).

6. OBJECTS AND EVENTS OF INTEREST

The majority of the objects in the ASAS-SN sample are newly discovered M dwarfs with typical colors and activity levels. Here we discuss M dwarfs with previous data and the peculiar objects observed as part of the ASAS-SN M-dwarf project.

6.1. *GJ 3039*

GJ 3039 (LP 525-39) was first identified as an Hα emitting, high-proper motion source (Stephenson 1986a,b) before it was included in the third catalog of nearby stars (Gliese & Jahreiß 1991) and assigned an M4 spectral type (Reid et al. 1995). McCarthy et al. (2001) found a companion to GJ 3039 with a separation of 0.″73 ($\sim$ 30 AU) and similar colors, but a magnitude difference of 0.7 in J-band. Schlieder et al. (2012) identified GL 3039 as a candidate member of the β Pictorus young moving group due to a combination of kinematics detected emission at X-ray in UV wavelengths. Previous photometric monitoring of GJ 3039 (Messina et al. 2016) identified two small R-band flares. The ASAS-SN light curve of GJ 3039 also includes a few small ($\Delta V < -0.2$) flares, but none as large as the $\Delta V = -1.0$ flare examined here.

6.2. *ASASSN-13cb (SDSS1022+19)*

SDSS1022+19 was observed to flare in Fall 2013. Because the flare was both very large, and occurred on a very red object, follow-up observations were obtained rapidly and the object and its flare were analyzed by Schmidt et al. (2014), who classified it as a field age M8 dwarf with a lower limit flare energy of $\log(E_V) = 34.4$ [log(erg)]. We re-analyze the flare here

using an updated fitting procedure and the Davenport et al. (2014b) flare template (unavailable during the original analysis) and find an energy of $\log(E_V) = 33.7$ [log(erg)]. As discussed in Section 3, this fit does not show strong agreement with the late-stage ($\sim$ 2 hours later) decay observed for ASASSN-13cb, but does show agreement with the flare lightcurve calculated from the *Kepler* relationship between timescale and energy.

6.3. *ASASSN-15af (2M0518−05)*

ASASSN-15af was identified as T Tauri star 2MASS J05181685−0537300 (2M0518−05) as part of a photometric Hα survey in Orion (Wiramihardja et al. 1991). A spectrum from Lee & Chen (2007) revealed many emission lines, including Hα (EW= −57.3Å), OI 6300Å, Fe 4924Å, Ca H&K, and He I (5876Å), sufficient to classify 2M0518−05 as a T Tauri star, but there was no discussion of the continuum or spectral type. It is marked as a likely T Tauri star in the ASAS-SN transient page, but was placed on our observing list due to its red colors. We obtained three spectra of 2M0518−05 on 2016 August 2 and on 2017 Feb 23, shown in Figure 7.

The spectrum of 2M0518−05 is shown compared to an M6 template spectrum; while the blue continuum is not consistent with an M6 dwarf, there are molecular bands throughout the redder portion of the spectrum (7000–9000Å) that are well-matched by the template spectrum. The subtracted spectrum shows less evidence of these bands, and appears to primarily be composed of blue continuum and emission lines. While the combination of emission lines and blue continuum would be expected in a magnetically-triggered flare, the line profiles are wider than those typically found during a flare event, most notably the Hα emission, which is $\sim$50Å wide and double peaked. It is more likely that the observed spectra are elevated due to accretion and other star formation processes.
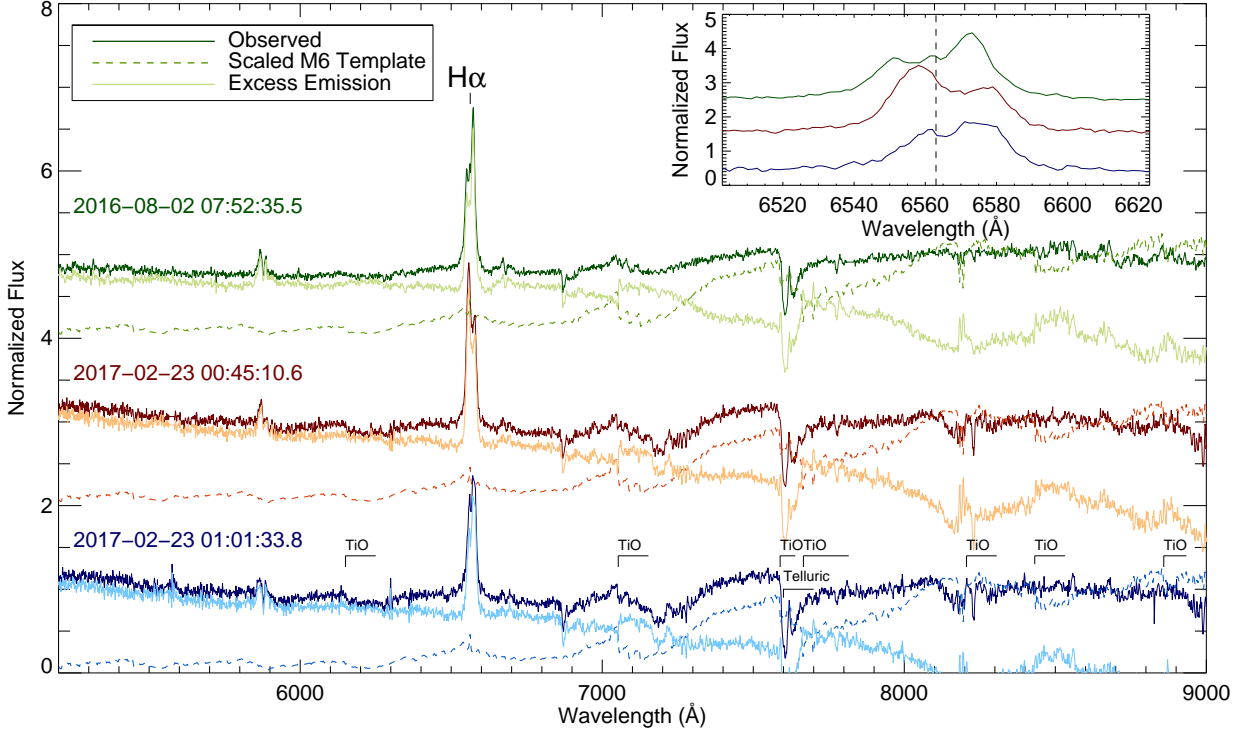
Figure 7. Three spectra of T Tauri star 2M0518−05 (dark green, red, and blue lines), observed on 2016 Aug 2 and 2017 Feb 23, compared to an M6 dwarf template (green, red and blue dashed lines). The T Tauri spectra with the M6 dwarf template subtracted (light green, red, and blue lines) show excess emission similar to that expected from flares, including elevated blue continuum and emission lines. The TiO features found in both the template and 2M0518−05 are labeled in the bottom spectrum. The Hα line profiles (shown in the inset) are wide, variable, and multi-peaked, providing additional evidence that this object is showing activity primarily due to accretion rather than magnetic fields.

The ASAS-SN light curve of 2M0518−05 shows at least fourteen distinct outburst events, including the initial 2015 event that triggered the observations (all shown in Figure 8). We obtained two additional photometric points for the object, obtaining $V = 17.2$ mag both times. This is likely to be the quiescent value, as ASAS-SN detects 2M0518−05 in quiescence with a similar magnitude when the observing conditions are particularly good. While some of the outburst events were only detected on a single day and could be consistent with either magnetically induced flares or accretion, others last for multiple days at a time and so are far more likely to be accretion events. In addition to this activity, 2M0518−05 also shows strong variation in the CRTS database and has excess

UV emission (Sanchez et al. 2014). Because any magnetic activity on this object is difficult to separate from accretion, we exclude 2M0518−05 from the sample of flaring M dwarfs.

6.4. *ASASSN-16ae (SDSS0533+00)*

SDSS0533+00 was observed to flare in January 2016. Because the flare was both very large, and occurred on a very red object, follow-up observations were obtained rapidly. The object and its flare were analyzed by Schmidt et al. (2016), who classified it as a field age L0 dwarf with a minimum V-band flare energy of $\log(E_V/\mathrm{ergs}) = 33.7$. The updated fitting method used in this work also measures $\log(E_V/\mathrm{ergs}) = 33.7$, though using a different distance; Schmidt et al. (2016) used a
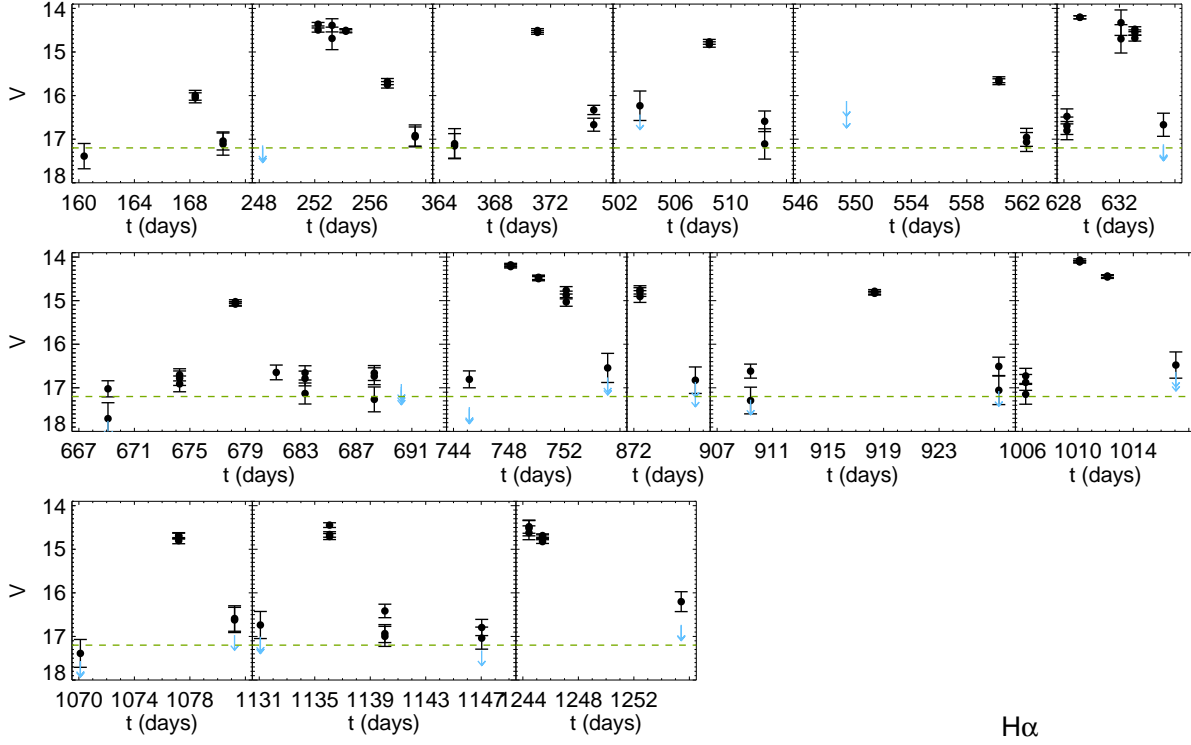
Figure 8. V magnitude as a function of time for 14 outbursts from 2M0518−05. A possible quiescent level ($V = 17.2$) is shown (green dashed line) as well as the detections (filled circles) and upper limits (blue arrows). Time is given in days since 2014 Jan 1. Many outbursts may have lasted a similar time to a magnetically induced stellar flare (hours), but the light curve of 2M0518−05 also features a few multi-day outbursts that are most likely related to accretion events.

combination of eight different photometric and spectrophotometric distances with a final result of d=95.5 pc, while here we adopt d=77.9 pc based on the $M_i/i − z$ relation from Schmidt (2018, in prep.).

6.5. *ASASSN-16hl*

ASASSN-16hl (2MASS J16045515-7223199) was marked in the ASAS-SN transients database as a CV or an outburst from a red star, and was selected for follow-up due to its particularly red colors in 2MASS and WISE. The spectrum of ASASSN-16hl (shown in Figure 9) has molecular absorption similar to an M1 dwarf, but has a blue continuum and emission lines similar to a flare or other hot outburst. No other spectra were obtained, so it is unclear whether the single spectrum represents a continuous or transient state.
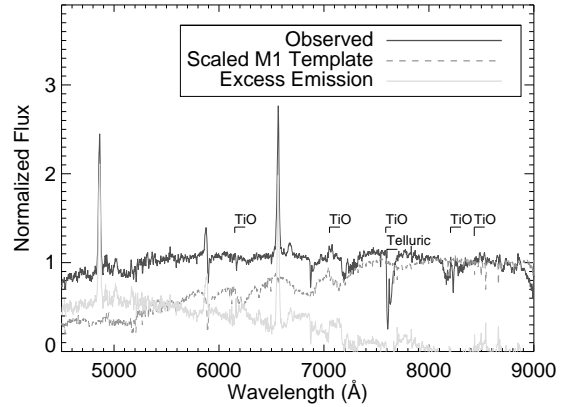
Figure 9. Spectrum of ASASSN-16hl, a red object with multiple outbursts in the ASAS-SN database. The object is compared to an M1 template and is possibly a late-type star with additional emission in the continuum. The TiO features found in both the template and ASASSN-16h are labeled.
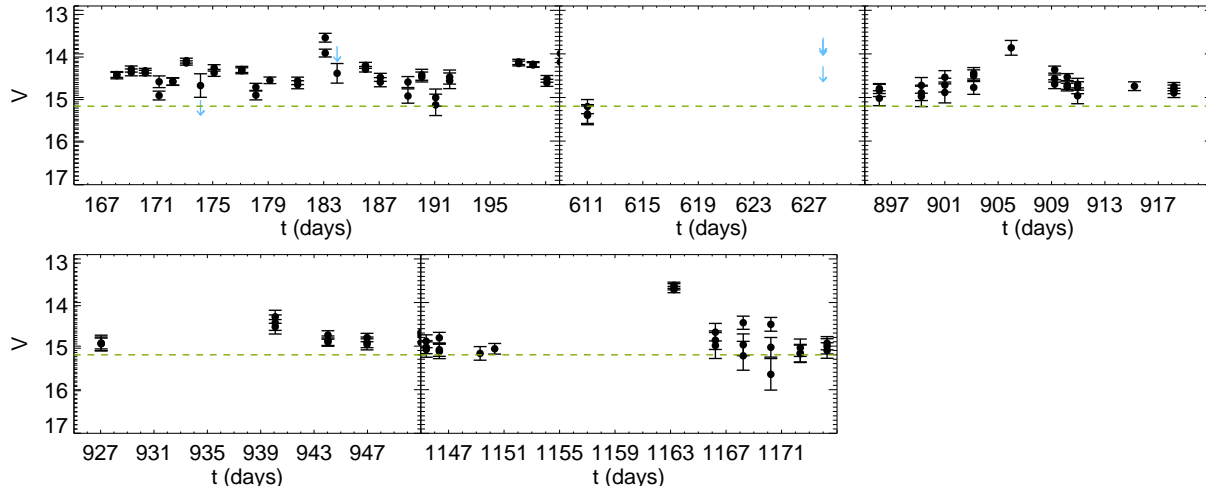
Figure 10. V magnitude as a function of time for three outbursts and two long timescale elevations of ASASSN-16hl.

The light curve of ASASSN-16hl shows multiple strong outbursts, including a strong event that resembles a flare (in part due to the lack of observations within a few days), two multi-day outbursts, and a few smaller, longer outbursts (shown in Figure 10). Our follow-up photometry yielded a magnitude of $V = 14$, which is likely to have been during another outburst. The median ASAS-SN value is $V = 16.1$ mag, which is possibly the quiescent value. In further support that this is a peculiar, young object, the WISE database flagged the photometry as variable, and a Simbad search reveals a possibly associated X-ray source in ROSAT within a few arcseconds. ASASSN-16hl is most likely a previously unclassified young star. We used the Banyan Σ tool[5] (Gagné et al. 2018) to check if it is a member of any young moving group or association, and found it is most likely a field star.

7. SUMMARY

We selected 55 candidate flaring M dwarfs from ASAS-SN and performed follow-up spectroscopy and photometry on 53 of them, identifying four as peculiar objects, and 49 as K,

M, or L dwarfs. From these 49 stars we identified 55 total flares. The flares have lower limits on their V-band energies that range from $\log(E_V/\mathrm{ergs}) = 32$ to 35, placing them among some of the strongest M-dwarf flares detected. The flare stars tend to have more and stronger chromospheric activity (as characterized by Hα emission) than typical field M dwarfs, but are not an older population than field M dwarfs.

If we adopt the Maehara et al. (2012) definition of super flares (energies greater than 10^{33} erg), the majority of the stellar flares observed by ASAS-SN (44 of 55) fall above that cut in the V-band, and with *Kepler* energies approximately 1.9 times larger than those in V-band, 50 of the 55 flares would fall into the super flare category. With its bright magnitude range and full sky coverage, ASAS-SN is well-suited to detecting these flares. The few largest ASAS-SN flares previously analyzed are larger than the biggest flares that have been examined in detail ($\sim 10^{34}$ erg; Hawley & Pettersen 1991; Kowalski et al. 2010), but still smaller than the largest found on M dwarfs in the Davenport (2016) flare catalog, which range up to $\log(E_{Kepler}) = 36$ [log(erg)].

ASAS-SN and similar sparse cadence surveys have the potential to uniquely observe an un-

biased sample of nearby M dwarfs, detecting the largest flares and allowing us to characterize those flares as a population. As observations continue, we will continue to add to our understanding of M dwarf flares. This is essential not only to understand the relationship between flare activity and underlying stellar properties such as mass, rotation, and age, but also to estimate how frequently life on extrasolar planets may be threatened by the largest flares.

In the last half of 2017 ASAS-SN deployed three additional units in Texas, South Africa, and Chile and by the end of 2018 we will deploy a sixth unit to China. These new units both increase our cadence and decrease our vulnerability to weather. With the 5-unit ASAS-SN we cover the entire visible sky every 20 hours, increasing the number of M-dwarf flares we recover dramatically. Using the data presented here combined with additional flares from the expanded survey, we plan to derive rates of the largest M dwarf flares from ASAS-SN in a follow-up work.

REFERENCES

Abazajian, K. N., Adelman-McCarthy, J. K., Agüeros, M. A., et al. 2009, ApJS, 182, 543

Aihara, H., Allende Prieto, C., An, D., et al. 2011, ApJS, 193, 29

Anfinogentov, S., Nakariakov, V. M., Mathioudakis, M., Van Doorsselaere, T., & Kowalski, A. F. 2013, ApJ, 773, 156

Bailer-Jones, C. A. L., Rybizki, J., Fouesneau, M., Mantelet, G., & Andrae, R. 2018, ArXiv e-prints, arXiv:1804.10121

Bochanski, J. J., Hawley, S. L., Covey, K. R., et al. 2010, AJ, 139, 2679

Bochanski, J. J., Hawley, S. L., & West, A. A. 2011, AJ, 141, 98

Bochanski, J. J., West, A. A., Hawley, S. L., & Covey, K. R. 2007, AJ, 133, 531

Borucki, W. J., Koch, D., Basri, G., et al. 2010, Science, 327, 977

Browning, M. K. 2008, ApJ, 676, 1262

Browning, M. K., Miesch, M. S., Brun, A. S., & Toomre, J. 2006, ApJL, 648, L157

Cruz, K. L., Reid, I. N., Kirkpatrick, J. D., et al. 2007, AJ, 133, 439

Davenport, J. R. A. 2016, ApJ, 829, 23

Davenport, J. R. A., Hawley, S. L., Hebb, L., et al. 2014a, ApJ, 797, 122

Davenport, J. R. A., Ivezić, Ž., Becker, A. C., et al. 2014b, MNRAS, 440, 3430

Davis, A. B., Shappee, B. J., Archer Shappee, B., & ASAS-SN. 2015, in American Astronomical Society Meeting Abstracts, Vol. 225, American Astronomical Society Meeting Abstracts, 344.02

Dong, S., Shappee, B. J., Prieto, J. L., et al. 2016, Science, 351, 257

Dressler, A., Bigelow, B., Hare, T., et al. 2011, PASP, 123, 288

Faherty, J. K., Burgasser, A. J., Cruz, K. L., et al. 2009, AJ, 137, 1

France, K., Loyd, R. O. P., Youngblood, A., et al. 2016, ApJ, 820, 89

Gagné, J., Mamajek, E. E., Malo, L., et al. 2018, ApJ, 856, 23

Gaia Collaboration, Brown, A. G. A., Vallenari, A., et al. 2018, ArXiv e-prints, arXiv:1804.09365

Gizis, J. E., Burgasser, A. J., Berger, E., et al. 2013, ApJ, 779, 172

Gizis, J. E., Monet, D. G., Reid, I. N., et al. 2000, AJ, 120, 1085

Gliese, W., & Jahreiß, H. 1991, Preliminary Version of the Third Catalogue of Nearby Stars, Tech. rep.

Hawley, S. L., Davenport, J. R. A., Kowalski, A. F., et al. 2014, ApJ, 797, 121

Hawley, S. L., & Pettersen, B. R. 1991, ApJ, 378, 725

Henden, A., & Munari, U. 2014, Contributions of the Astronomical Observatory Skalnate Pleso, 43, 518

Henry, T. J., Subasavage, J. P., Brown, M. A., et al. 2004, AJ, 128, 2460

Herczeg, G. J., Dong, S., Shappee, B. J., et al. 2016, ApJ, 831, 133

Hilton, E. J. 2011, PhD thesis, University of Washington

Hilton, E. J., West, A. A., Hawley, S. L., & Kowalski, A. F. 2010, AJ, 140, 1402

Holoien, T. W.-S., Shappee, B. J., Stanek, K. Z., et al. 2014a, The Astronomer's Telegram, 6168

Holoien, T. W.-S., Prieto, J. L., Bersier, D., et al. 2014b, MNRAS, 445, 3263

Holoien, T. W.-S., Kochanek, C. S., Prieto, J. L., et al. 2016a, MNRAS, 463, 3813

—. 2016b, MNRAS, 455, 2918

Holoien, T. W.-S., Brown, J. S., Stanek, K. Z., et al. 2017a, ArXiv e-prints, arXiv:1704.02320

Holoien, T. W.-S., Stanek, K. Z., Kochanek, C. S., et al. 2017b, MNRAS, 464, 2672

Holoien, T. W.-S., Brown, J. S., Stanek, K. Z., et al. 2017c, MNRAS, 467, 1098

Howell, S. B., Sobeck, C., Haas, M., et al. 2014, PASP, 126, 398

Kay, C., Opher, M., & Kornbleuth, M. 2016, ApJ, 826, 195

Khodachenko, M. L., Ribas, I., Lammer, H., et al. 2007, Astrobiology, 7, 167

Kochanek, C. S., Shappee, B. J., Stanek, K. Z., et al. 2017, PASP, 129, 104502

Kowalski, A. F., Hawley, S. L., Hilton, E. J., et al. 2009, AJ, 138, 633

Kowalski, A. F., Hawley, S. L., Holtzman, J. A., Wisniewski, J. P., & Hilton, E. J. 2010, ApJL, 714, L98

Kowalski, A. F., Hawley, S. L., Wisniewski, J. P., et al. 2013, ApJS, 207, 15

Lacy, C. H., Moffett, T. J., & Evans, D. S. 1976, ApJS, 30, 85

Lammer, H., Lichtenegger, H. I. M., Kulikov, Y. N., et al. 2007, Astrobiology, 7, 185

Lang, D., Hogg, D. W., Mierle, K., Blanton, M., & Roweis, S. 2010, AJ, 139, 1782

Lee, H.-T., & Chen, W. P. 2007, ApJ, 657, 884

Li, K.-L., Metzger, B. D., Chomiuk, L., et al. 2017, Nature Astronomy, 1, 697

Lin, R. P., & Hudson, H. S. 1976, SoPh, 50, 153

Lindegren, L., Hernandez, J., Bombrun, A., et al. 2018, ArXiv e-prints, arXiv:1804.09366

Luger, R., & Barnes, R. 2015, Astrobiology, 15, 119

Maehara, H., Shibayama, T., Notsu, S., et al. 2012, Nature, 485, 478

Martini, P., Stoll, R., Derwent, M. A., et al. 2011, PASP, 123, 187

McCarthy, C., Zuckerman, B., & Becklin, E. E. 2001, AJ, 121, 3259

Messina, S., Naves, R., & Medhi, B. J. 2016, NewA, 48, 5

O'Malley-James, J. T., & Kaltenegger, L. 2017, MNRAS, 469, L26

Osten, R. A., Hawley, S. L., Allred, J. C., Johns-Krull, C. M., & Roark, C. 2005, ApJ, 621, 398

Pineda, J. S., West, A. A., Bochanski, J. J., & Burgasser, A. J. 2013, AJ, 146, 50

Pogge, R. W., Atwood, B., Brewer, D. F., et al. 2010, in Society of Photo-Optical Instrumentation Engineers (SPIE) Conference Series, Vol. 7735, Society of Photo-Optical Instrumentation Engineers (SPIE) Conference Series

Ramsay, G., & Doyle, J. G. 2015, MNRAS, 449, 3015

Reid, I. N., Hawley, S. L., & Gizis, J. E. 1995, AJ, 110, 1838

Rodríguez, R., Schmidt, S. J., Jayasinghe, T., et al. 2018, Research Notes of the American Astronomical Society, 2, 8

Sanchez, N., Inés Gómez de Castro, A., Lopez-Martinez, F., & López-Santiago, J. 2014, A&A, 572, A89

Schlieder, J. E., Lépine, S., & Simon, M. 2012, AJ, 143, 80

Schmidt, S. J. 2018, in prep.

Schmidt, S. J., Hawley, S. L., West, A. A., et al. 2015, AJ, 149, 158

Schmidt, S. J., Prieto, J. L., Stanek, K. Z., et al. 2014, ApJL, 781, L24

Schmidt, S. J., Shappee, B. J., Gagné, J., et al. 2016, ApJL, 828, L22

Segura, A., Walkowicz, L. M., Meadows, V., Kasting, J., & Hawley, S. 2010, Astrobiology, 10, 751

Shappee, B. J., Prieto, J. L., Grupe, D., et al. 2014, ApJ, 788, 48

Shappee, B. J., Stanek, K. Z., Schmidt, S., et al. 2016a, The Astronomer's Telegram, 8553

Shappee, B. J., Piro, A. L., Holoien, T. W.-S., et al. 2016b, ApJ, 826, 144

Silverberg, S. M., Kowalski, A. F., Davenport, J. R. A., et al. 2016, ApJ, 829, 129

Simonian, G., Stanek, K. Z., Schmidt, S., et al. 2016, The Astronomer's Telegram, 8803

Skrutskie, M. F., Cutri, R. M., Stiening, R., et al. 2006, AJ, 131, 1163

Stanek, K. Z., Shappee, B. J., Kochanek, C. S., et al. 2013a, The Astronomer's Telegram, 5276, 1

—. 2013b, The Astronomer's Telegram, 5186

Stephenson, C. B. 1986a, AJ, 92, 139

—. 1986b, ApJ, 300, 779

Tilley, M. A., Segura, A., Meadows, V. S., Hawley, S., & Davenport, J. 2017, ArXiv e-prints, arXiv:1711.08484

van Dokkum, P. G. 2001, PASP, 113, 1420

Vida, K., Kriskovics, L., Oláh, K., et al. 2016, A&A, 590, A11

Walkowicz, L. M., Basri, G., Batalha, N., et al. 2011, AJ, 141, 50

West, A. A., & Hawley, S. L. 2008, PASP, 120, 1161

West, A. A., Hawley, S. L., Bochanski, J. J., et al. 2008, AJ, 135, 785

West, A. A., Morgan, D. P., Bochanski, J. J., et al. 2011, AJ, 141, 97

Wiramihardja, S. D., Kogure, T., Yoshida, S., et al. 1991, PASJ, 43, 27

Wright, E. L., Eisenhardt, P. R. M., Mainzer, A. K., et al. 2010, AJ, 140, 1868

York, D. G., Adelman, J., Anderson, Jr., J. E., et al. 2000, AJ, 120, 1579

Youngblood, A., France, K., Parke Loyd, R. O., et al. 2017, ApJ, 843, 31